An experimental study on the spatiotemporal evolution of sand waves/ripples in turbulent boundary layer airflow

Yang Liu (刘洋), Xianyang Jiang (江贤洋), Cunbiao Lee (李存标), et al.

COLLECTIONS

EP   This paper was selected as an Editor's Pick

View Online   Export Citation   CrossMark

ARTICLES YOU MAY BE INTERESTED IN

On respiratory droplets and face masks
Physics of Fluids **32**, 063303 (2020); https://doi.org/10.1063/5.0015044

Flow structures in transitional and turbulent boundary layers
Physics of Fluids **31**, 111301 (2019); https://doi.org/10.1063/1.5121810

Visualizing the effectiveness of face masks in obstructing respiratory jets
Physics of Fluids **32**, 061708 (2020); https://doi.org/10.1063/5.0016018

Physics of Fluids
Special Topic: Hydrogen Flame and Detonation Physics
Submit Today!

An experimental study on the spatiotemporal evolution of sand waves/ripples in turbulent boundary layer airflow ⓔⓟ

Yang Liu (刘洋),[1,2,a] ⓘⒹ **Xianyang Jiang (江贤洋),**[3] ⓘⒹ **Cunbiao Lee (李存标),**[3] ⓘⒹ **and Hui Hu (胡晖)**[1,a] ⓘⒹ

AFFILIATIONS

[1] Department of Aerospace Engineering, Iowa State University, Ames, Iowa 50011-2271, USA
[2] Department of Engineering, East Carolina University, Greenville, North Carolina 27858, USA
[3] State Key Laboratory for Turbulence and Complex Systems, Peking University, Beijing 100871, China

[a] **Authors to whom correspondence should be addressed:** liuya19@ecu.edu and huhui@iastate.edu

ABSTRACT

An experimental study was conducted to investigate the spatiotemporal evolution of sand waves/ripples submerged in a turbulent boundary layer airflow. While a digital image projection technique was applied to achieve temporally resolved measurements of the dynamically evolving sand surface morphology, a combined particle tracking/imaging velocimetry technique was also used to reveal the two-phase (i.e., air–sediment) flow field during the dynamic sand wave/ripple evolution process. It was found that the sand bed surface would evolve from initial random three-dimensional (3D) sand wavelets to two-dimensional (2D) sand waves and further into well-organized sequences of 3D chevron-shaped sand ripples that are separated by longitudinal streaks, when exposed to the turbulent boundary layer airflow. A discrepancy of the local sand wave propagation at different transverse locations was revealed based on the wavelet analysis of the time-series of the sand bed height variation, which was suggested to contribute to the formation of the 3D chevron-shaped sand ripples. It was also found that the evolving sand waves/ripples could dramatically affect the near-bed two-phase (i.e., air–sediment) flow structures as indicated by the dramatically disturbed air–sediment flow structures. By correlating the sand surface profiles and the near-surface sand particle velocity patterns, a complete description of the dynamic sand bedform evolution was revealed with five dominant phases being defined: (I) initial strengthening phase, (II) transition phase, (III) ripple-modulated re-strengthening phase, (IV) stabilizing phase, and (V) longitudinal phase.

Published under license by AIP Publishing. https://doi.org/10.1063/1.5144522

I. INTRODUCTION

Sand ripples and waves are commonly observed geological morphologies in nature, either in the inland desert areas or on the bed of sandy shallow seas. Various sand patterns have been observed in nature, which include waves, ripples, subaqueous dunes, antidunes, chevrons, and alternate bars.[1,2] The formation of these sand patterns is generally caused by the emission, transport, and deposition of sand and dust, driven by fluid flow in both aeolian and fluvial environments. The research on aeolian sand ripples can be dated back to the late 1890s, when Darwin[3] and Cornish[4] found the existence of lee-side eddies to move sand grains to form sand ripples and dunes. However, the later observations and experiments revealed that there is no direct linkage between the lee-side eddies and the sand ripple formation or development.[5–7] Instead, the sorting mechanism (i.e., natural sifting of sand grains by different sizes) was proposed to account for the aeolian sand ripple formation.[8–10] Depending on the sand particle size and wind speed, several transportation modes of aeolian ripples were proposed to describe the complex interactions between the boundary layer airflow and the erodible sand surface. When the atmospheric wind is sufficiently strong, small sand particles can be moved and lifted by fluid flow, hopping along the soil surface in a process known as saltation.[11] The impacts of saltating particles can mobilize larger particles, leading to the process of reptation,[12] during which the particles settle back to the soil after a short hop. By correlating the sand ripple wavelength

and the characteristic path length in sand saltation, it was suggested that the ripple height and shape are determined by the surface sand grading and the incidence angle of saltation.[13–15] Later in the 1990s, a theoretical model of sand ripple formation was developed, involving two sub-processes, i.e., saltation with a long trajectory vs reptation with a short trajectory.[16] It was revealed that the growth of sand ripples is essentially caused by the spatial variations of sand mass flux due to the reptating population.[17]

Another genre of elucidating the aeolian sand ripple formation is associated with the instability of the fluid–sediment flow system, in which the sediment is viewed as a viscous fluid and the formation of sand ripples is considered to be a result of Kelvin–Helmholtz instability of two shear fluids with different densities.[18] By simplifying the problem as a homogeneous ideal fluid over an erodible, sinusoidal bed, it was found that there is a spatial lag between the maximum bed velocity and the maximum sediment transport rate.[19] The stability theories were then developed based on the real fluid with internal frictions.[20] Two separated instability modes were proposed with consideration of realistic turbulent flow close to the bed, i.e., one is dependent on the local roughness of the bed and the other is associated with the depth of flow.[21] It was found that the viscous shear can cause particle resuspension and the effect of the viscosity profile on the stability characteristics could be much more dramatic than that of the density profile.[22] Recently, a different approach of linear stability analysis was performed using direct numerical simulations,[23] in which the phase lag between the bed topology and the sediment flux was obtained from the three-dimensional turbulent simulations. It was found that while the Froude number is the critical controlling parameter in the early linear development of ripples, the particle Reynolds number becomes more dominant during the equilibrium stage.

Turbulent bursting, which is characterized as quasiperiodic cycles of ejection of fluid away from the wall followed by a high-speed sweep moving fluid toward the wall,[24] is another possible mechanism to cause erosion and deposition of sediments.[25] By correlating the turbulent structures and the topographic features of the sediment bed, it was found that turbulent bursting plays an important role in entrainment and suspension of mobile sediments.[26] The formation of entrainment patches as well as the ripple development was illustrated with the "grouped sweep" model developed based on the streak bursting cycle.[27] In recent years, it was also revealed that turbulent sweeps in the near-bed region are the primary mechanism for destabilizing the sand bedform.[28] Along with the advancement of turbulence modeling in recent years, more details about the relationship between turbulent bursting and sediment movement were extracted by applying the quadrant analysis and turbulence kinetic energy (TKE) budget methods.[29–31] A recent study by Groom and Friedrich[32] revealed that while the decrease in sand wave/ripple elevation could lead to an increase in the average near-bed velocity, the increase in the sand form roughness would result in an increase in both turbulence intensity and turbulent production (TKE). It was also found that the dispersive kinetic energy diffusion is substantial within the roughness sublayer.[33]

Though the mechanisms controlling the emergence of sand bedforms have been extensively investigated over the past years,[28,34–39] the evolutionary particulars of the sand bedforms and the complex interactions between the dynamically evolving sand ripples/waves and the boundary layer airflow are still not revealed

due to the lack of knowledge about the transient surface morphological details and the near-surface air–sediment flow characteristics during the dynamic courses of sand ripple formation and development. Advanced experimental techniques, which are capable of making time-resolved, quantitative measurements of the surface morphologies of wind-driven sand ripples/waves, are highly desirable to provide a complete description of the sand bedform formation and evolution process. In recent years, various measurement techniques have been developed to achieve quantitative, non-intrusive measurements of thickness distribution/surface morphologies of different substances,[40–45] among which the novel digital image projection (DIP) technique developed by Zhang et al.[45] and Liu et al.[46] has been demonstrated to be a very reliable measurement tool to reconstruct the complex three-dimensional (3D) geometrical profiles of various objects with great resolutions in both temporal and spatial dimensions. In the present study, the DIP technique was implemented to provide temporally resolved measurements of the sand surface morphology to quantify the transient behaviors of sand ripples/waves submerged in a turbulent boundary layer airflow. Based on the quantitative DIP measurements, a complete evolution process of the sand bedform was revealed, with various sand ripple/wave structures (i.e., in terms of wave shape, frequency, and wave number) being characterized clearly and quantitatively in both time and space scales. In addition to the DIP measurements, a series of combined particle tracking/imaging velocimetry (PTV/PIV) measurements were also conducted in the present study to reveal the air–sediment velocity field during the dynamic sand wave/ripple formation process. Then, by correlating the sand bed surface profiles and the near-bed sand particle flow field, a complete description of the dynamical mechanisms controlling the sand bedform evolution was revealed. To the best knowledge of the authors, this is the first effort of its kind to quantitatively define the evolutionary details of the aeolian sand bedform driven by the turbulent boundary layer airflow.

In the context that follows, the experimental methods to quantify the sand surface morphology and the two-phase flow field are described at first. Then, the key parameters that define the dynamic air–sediment flow interactions and the sand surface morphologies are introduced. Based on the quantitative measurements of the sand surface morphologies, both the temporal evolution and the spatial variation of the ripple-modulated sand surfaces are extracted and analyzed. In addition, the characteristics of the dynamically evolving sediment-air flow fields during the sand wave/ripple formation process are also revealed in great details.

II. EXPERIMENTAL METHODS

The experimental study was performed in the Low-disturbance Wind Tunnel located at the College of Engineering of Peking University (i.e., PKU-LWT). The PKU-LWT is a closed-circuit wind tunnel with two test sections that are equipped with optically transparent windows, i.e., one has a cross section of 1.5 m in width × 1.5 m in height and the other has a cross section of 1.0 m in width × 1.0 m in height. The wind tunnel has two contraction sections upstream of each test section with a set of honeycombs and screen structures installed ahead of the first contraction section to provide uniform, low turbulence airflow into the test sections. All the experiments in

the present study were performed in the smaller test section (i.e., 1.0 m in width × 1.0 m in height), which has a capacity of generating a maximum wind speed of 50 m/s.

A. Digital image projection (DIP) technique

The DIP technique used in the present study is a structured light technique, which relies on actively projecting known light patterns onto an object and extracting 3D surface shapes from the images of the projected light patterns captured from one or more points of view.[43] Figure 1 shows the schematic to illustrate the technical basis of the DIP technique. As shown in Fig. 1(a), a digital projector is used to project image patterns with known characteristics onto a test object of interest (e.g., the sand surface in the present study). Due to the complex surface shape of the test object, the projected image patterns will deform when observed from a different perspective other than the projection axis. The projection unit, the image acquisition unit, and the three-dimensional object form a triangulation base. If the corresponding points between the camera (A) and the projector (C) are identified through a calibration procedure, the 3D shape of the test object can be obtained through an analysis of the triangulation of $\triangle ABC$. It should be noted that the correspondence for the DIP technique used in this study is established by finding the displacement vectors between corresponding points in the distorted images (i.e., the images acquired with the ripple/wave features formed on the sand surface) and a reference image (i.e., the image acquired without any ripples/waves on the measurement plane) by using a spatial cross correlation image processing algorithm.[45,46] This is very different from the most-commonly used fringe-based structured light technique, in which the 3D profile of the test object with respect to the reference plane is retrieved based on the measured phase changes between the modulated fringe patterns and those in the reference image.[43]

For the DIP technique used in the present study, the 3D shape of the measured object is restructured based on the displacement map of the corresponding points between the distorted images and the reference image. Figure 1(b) shows the diagram of the DIP technique for displacement-to-height conversion. A reference plane with a height 0 in the Z-direction is used as the reference surface for all

subsequent measurements. The arbitrary point "M" in the captured image corresponds to point "N" in the projected image, and point "D" on the object surface. From the projector's point of view, point "D" on the object surface has the same position as point "A" on the reference plane. However, from the point of view of the image recording camera, point "D" on the object surface images will be at the same position as point "C" on the reference plane. Therefore, the same point "N" in the projected image will be recorded as point "A" in the reference image (i.e., the image acquired with the sand surface being flat) and point "C" in the distorted image (i.e., the image acquired with the ripples/waves formed over the sand surface). The distance between point "A" and point "C" represents the displacement of the same point "N" between the distorted and reference images. Assume the distance between point "M" and point "N" is d, and the reference plane is parallel to the plane of devices with a distance s between them. Similar triangles can be formed between $\triangle MND$ and $\triangle CAD$; therefore,

$$\frac{d}{\overline{CA}} = \frac{s - \overline{BD}}{\overline{BD}} = \frac{s}{\overline{BD}} - 1. \tag{1}$$

Because the distance s is usually much larger than $\overline{BD}$, this equation can be simplified as

$$Z(x,y) = \overline{BD} \approx \frac{s}{d}\overline{CA} = K\overline{CA}. \tag{2}$$

It should be noted that because the values of s and d are fixed for a given DIP setup, K will be a constant for a given DIP system, which can be determined through a calibration procedure. Equation (2) shows a linear relationship between the measured displacement $\overline{CA}$ and the object height $Z(x, y)$. Therefore, the 3D shape of the test object can be determined quantitatively by measuring the displacements between the distorted and reference images at the points of interest. Further information about the implementation procedure and image processing algorithm for DIP measurements can be found in the studies by Zhang et al.[45] and Liu et al.[46]

Figure 2 shows the experimental setup used in the present study to quantify the transient sand wave/ripple formation and evolution process. As shown schematically in the figure, a sand bed was used
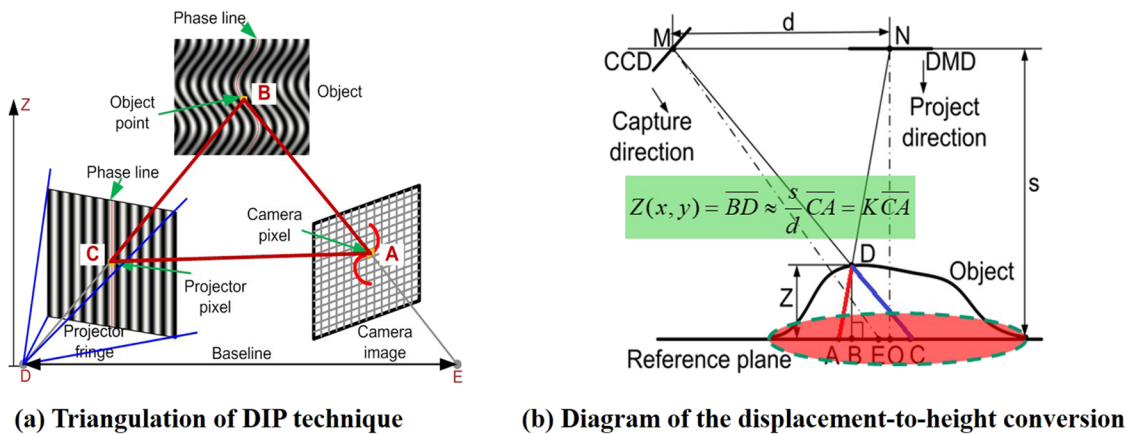

(a) Triangulation of DIP technique   **(b) Diagram of the displacement-to-height conversion**

FIG. 1. Technical basis of the digital imaging projection (DIP) technique: (a) triangulation of the DIP technique; (b) diagram of the displacement-to-height conversion.
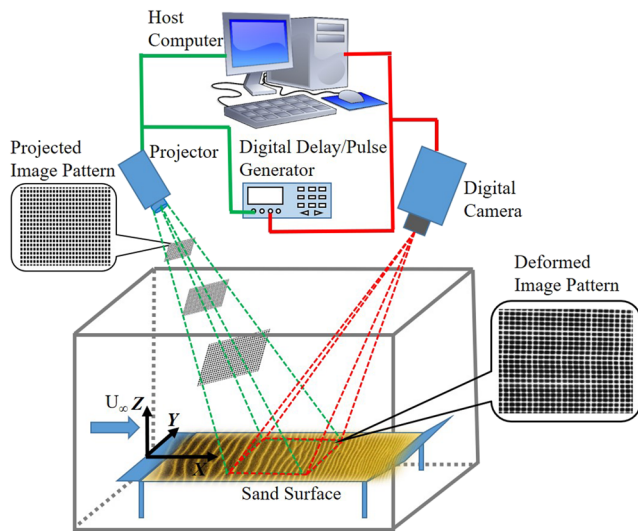
FIG. 2. Experimental setup for the DIP technique to quantify the aeolian sand ripple formation and development.

FIG. 3. Experimental setup for the PTV/PIV measurements of the sand particle flow field.

to load the sand grains. X, Y, and Z denote the streamwise, spanwise, and normal-to-surface directions, respectively. The sand bed, which is made of a hard plexiglass, has a groove of 1755 mm in length, 1000 mm in width, and 20 mm in depth to load the sand grains. The sand bed was mounted horizontally at a height of 430 mm from the bottom of the wind tunnel test section. An asymmetric leading-edge of 180 mm in length, with two cubic Bézier-curves connected at the nose tip, was designed following the approach as described by Fransson,[47] to ensure the minimum flow disturbance into the boundary layer airflow. A trailing edge flap was also designed to keep the stagnation point of the sand bed on the upper surface to compensate for the blockage effects caused by the support system.

As shown in Fig. 2, a commercially available projector (Dell DLP-M109S, of 858 × 600 pixels in resolution) was used to project a grid-patterned image onto the surface of the sand bed for the DIP measurements. A high-resolution digital camera (PCO sensi-cam QE 12 bit, of 1376 × 1040 pixels in resolution, produced by PCO Imaging company) with a 50 mm lens was used for the DIP image acquisition. The digital camera and the projector were synchronized with a digital delay generator (Stanford Research Systems, Inc., Model DG645). During the experiments, the DIP image acquisition was triggered to start right after the wind tunnel was turned on to start the sand emission/transport/deposition process, with 3600 images (i.e., 15 min in duration) being recorded in each test trial.

B. Particle tracking/imaging velocimetry (PTV/PIV)

In the present study, a combined particle tracking/imaging velocimetry (PTV/PIV) technique was also implemented to reveal the velocity structures of the two-phase (i.e., air–sediment) flow system. Figure 3 shows the experimental setup for the PTV/PIV measurements of the two-phase flow field. The illumination for the PTV/PIV measurements was provided from the top window by a
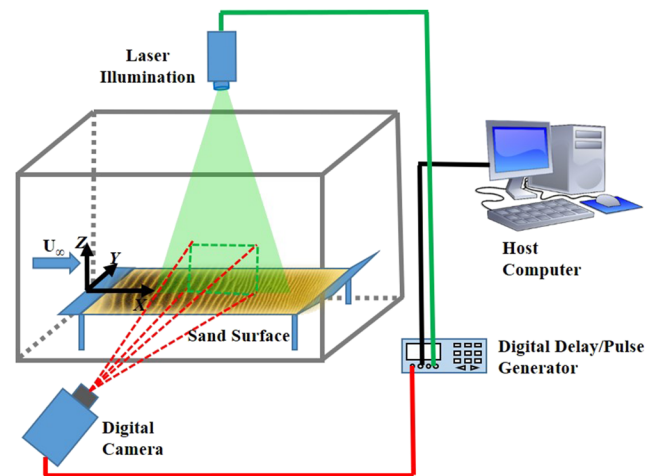
double-pulsed Nd:YAG laser adjusted on the second harmonic and emitting two pulses of 120 mJ at the wavelength of 532 nm. A set of convex and concave cylindrical lenses along with optical mirrors was used to generate a laser sheet with a thickness of 1 mm to illuminate the tracers in the near-bed flow field over the sand bed surface. A high-resolution digital camera (PCO sensicam QE 12 bit, of 1376 × 1040 pixels in resolution) with a 50 mm lens was used for PTV/PIV image acquisition with the axis of the camera being perpendicular to the laser sheet as shown in Fig. 3. The digital camera and the double-pulsed Nd: YAG laser were connected to a workstation (host computer) via a digital delay generator (Berkeley Nucleonics, Model 565), which controlled the timing of the laser illumination and the image acquisition. It should be noted that since the sand particles used in the present study have a relatively large diameter of ~0.21 mm, the corresponding Stokes number (i.e., Stk = $t_0 U_\infty / d_p$, where U_∞ is the incoming airflow velocity, d_p is the sand particle diameter, and t_0 is the relaxation time of the sand particle, $t_0 = \rho_p d_p^2 / 18 \mu_{air}$, where ρ_p is the density of the sand particle and μ_{air} is the dynamic viscosity of air) of the sand particles was estimated to be Stk > 200, which indicates that while the sand particles suspended in the air would be closely interacting with the gas flow, they would not follow the gas flow streamlines. Therefore, in the present study, specialized smoke oil was also used in the PIV measurements to generate droplet tracers of ~1 μm in diameter to seed the gas-phase flow structures in the air–sediment flow system.

In the present study, due to the limitation of the sampling frequency of the camera, the trajectories of the sand particles were not adequately obtained in the PTV measurements. In the meantime, since the bulk density of sand particles in the flow field is low and varies significantly as the time goes on, the spatial resolution of the PIV measurements is relatively low. Therefore, the algorithm of PIV + PTV is used to improve the spatial resolution of the vector field.[48,49] After the raw PTV/PIV images were acquired, a standard PIV post-processing (two pass cross correlation with an interrogation window size of 64 × 64 pixel² first and 32 × 32 pixel² second) was first executed to get an estimator of the local velocity of the sand

particles. Then, the resolution of the vector field was further refined by the detection and tracking of individual particles (i.e., PTV) with a vector field with regular grid (8×8 grid size) by applying a polynomial second order algorithm with additional filtering and smoothing procedures. It should be noted that after the instantaneous sand particle flow fields were derived, which contain a large number of noise components from the environment (background noise) and system (electrical noise), a series of Proper Orthogonal Decomposition (POD) analyses were performed to remove the noise components and extract the high energy modes of the flow structures.[50–52] In the present study, the dominant sand flow structures were reconstructed using the first 10 leading-order POD modes (which contain 40% of the total energy).

III. DESCRIPTIONS OF THE AIR–SEDIMENT FLOW SYSTEM AND SAND SURFACE MORPHOLOGY

A. Sand particles in airflow

In the present study, the size of the sand particles was selected to be d_p = 0.21 mm with a heterogeneity smaller than 1%, which represents the most commonly observed aeolian sand particles in nature.[10] Based on the air density at the room temperature (i.e., ρ_a = 1.225 kg/m^3) and the density of the sand grain as listed in Table I, the specific density of the sand particle is calculated to be

$$R = \frac{\rho_p - \rho_a}{\rho_a} = 1819. \tag{3}$$

Figure 4 shows a typical snapshot of sand particle translation velocities acquired in the PTV/PIV measurements. It is clearly seen that the sand particles are non-uniformly distributed in the measurement region, i.e., the sand particle concentration close to the sand bed surface is obviously higher than that in the outer layer. While most of the sand particles show a downward motion due to the gravity effect, there are still ascending sand particles, which indicates an evident saltation process over the sand bed surface. Following the work by Kulick et al.,[53] Aliseda et al.,[54] and Zhu et al.,[55] the particle bulk volume fraction, i.e., Φ_V, can be estimated using the box counting method as given in Eq. (4), where N_p is the number of identified sand particles within the measurement volume, e.g., the bright white dots shown in Fig. 4, Δx and Δz are the length and width of the measurement window, and Δy is the thickness of the laser-sheet thickness in the PTV/PIV measurements,

$$\Phi_V = \frac{\pi d_p^3 N_p}{6 \Delta x \Delta y \Delta z}. \tag{4}$$

The ratio between the gravity and viscous forces exerted on a suspending sand particle is usually described by the Galileo number,

TABLE I. Parameters related to the aeolian sand particles.

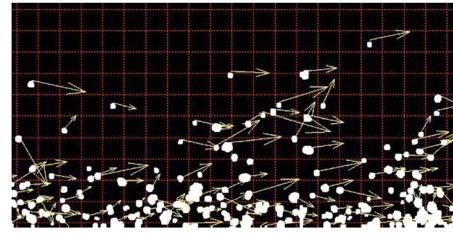| d_p (mm)	ρ_p (kg/m^3)	R	Ga	v_p (m/s)	Re_{p*}	τ_*	Φ_V
0.21	2230	1819	27.72	2.98	1.66	0.0038	5×10^{-3}

FIG. 4. A snapshot of sand particle translation velocities acquired in the PTV/PIV measurements.

which is given by

$$Ga = \left(gRd_p^3\right)^{1/2}/v, \tag{5}$$

where g is the gravitational acceleration and v is the kinematic viscosity of air.

The setting velocity of the sand particle, v_p, is estimated theoretically assuming that the sand particles are spheres with a diameter of d_p,

$$v_p = \frac{(\rho_p - \rho_a)gd_p^2}{18\mu}, \tag{6}$$

where μ is the dynamic viscosity of air.

When the sand bed is exposed to an aeolian environment, the shear velocity at the interface between the sand surface and the airflow, i.e., u_*, is a key parameter that determines the sand particle behaviors and sand surface morphology, which can be calculated using the following equation:

$$u_* = \sqrt{\tau_w/\rho_a} = \sqrt{\frac{\mu}{\rho_a} \frac{\partial u}{\partial z}\bigg|_{z=0}}, \tag{7}$$

where τ_w is the shear stress at the sand–air interface, which is a function of the velocity gradient, i.e., $\partial u/\partial z$, at the bottom of the air boundary layer.

Thus, the particle Reynolds number, Re_{p*}, can be calculated using the following equation:

$$Re_{p*} = \frac{u_* d_p}{v}. \tag{8}$$

The thickness of the viscous sublayer can be estimated as

$$H_* = \frac{5v}{u_*}. \tag{9}$$

Here, the dimensionless Shields shear stress is also introduced, which is defined as

$$\tau_* = \frac{u_*^2}{gRd_p}. \tag{10}$$

Since the shear stress at the sand–air interface can be calculated based on the boundary layer velocity profile that was also measured in the present study, all the parameters defined above are estimated and listed in Table I.

In the present study, while x, y, and z denote coordinates in the streamwise, transverse, and vertical directions, respectively, wall

units are used to normalize the various variables following the work of Niño and Garcia.[10] The wall units are characteristic scales formed using u_* and v, i.e., v/u_* represents a length scale, u_* represents a velocity scale, and v/u_*^2 represents a timescale. Variables with the subindex "+" are dimensionless with respect to the wall units.

B. Threshold shear velocity to initiate saltation

For the sand bed exposed to an aeolian environment, there is a threshold shear velocity initiating the saltation, which is usually derived as

$$u_{th} = A\sqrt{Rgd_p}, \tag{11}$$

where A is a dimensionless constant that is assumed to be 0.085 for the fluid threshold.[56,57] Thus, based on the parameter values listed in Table I, the threshold shear velocity is estimated to be u_{th} = 0.164 m/s, and the friction Reynolds number is calculated to be

$$Re_{f*} = \frac{\rho_a u_{th} d_p}{\mu} = 1.74. \tag{12}$$

The bulk Reynolds number is also calculated based on the sand bed width and bulk mean velocity, i.e., $Re_b = \frac{\rho_a U_\infty w}{\mu} = 4 \times 10^5$, where U_∞ is the bulk mean velocity and w is the width of the sand bed.

The impact threshold that defines the minimum shear stress of wind at which saltation can be sustained is lower than the fluid threshold due to the splashing particles that impact on the sedimentary bed and contribute more energy to move grains on the bed. As described by Bagnold,[11] the ratio between the impact threshold and the fluid threshold is about 0.8, which gives $u_{*,th}$ = 0.13 m/s.

Considering the inter-particle forces as suggested by Shao and Lu,[58] the threshold shear velocity is further calculated using the following equation:

$$u_{nth} = A_N \sqrt{\frac{\rho_p - \rho_a}{\rho_a} g d_p + \frac{\gamma}{\rho_a d_p}}, \tag{13}$$

where A_N is estimated to be A_N = 0.111, i.e., for the sand particle size larger than 200 μm; A_N^2 is recommended to be around 0.0123, according to the wind tunnel measurements.[59] γ is a scaled strength of inter-particle forces (i.e., $\gamma = 2.9 \times 10^{-4}$ Nm^{-1}) as given by Kok and Renno.[60] Thus, the threshold shear velocity considering the inter-particle forces is estimated to be u_{nth} = 0.25 m/s. While the ratio between the sand–fluid shear velocity and the freestream velocity in the fluid is estimated to be $u_*/U_\infty \approx 0.035$–0.05 as given by Tritton,[61] the corresponding threshold freestream velocity is estimated to range from $U_{\infty,th}$ = 5 m/s to $U_{\infty,th}$ = 7.1 m/s based on the sand particle parameters used in the present study.

C. Sand surface morphology

Following the previous work by Kidanemariam and Uhlmann,[62] the details of the sand surface morphology are extracted in terms of the sand bed height, H, sand height fluctuation, H', mean wavelength, λ, and mean amplitude, σ, of the sand wave/ripple patterns. It should be noted that due to the change in the sand bed height during the sand wave/ripple formation process in this study, the sand height fluctuation, H', is extracted by applying a de-trending procedure (i.e., sand height fluctuation with respect to the trending of bed height variation). For example, the local sand height fluctuation

in the time-series at $x = \hat{x}$, $H'(\hat{x}, t)$, is extracted using the following equation:

$$H'(\hat{x}, t) = H(\hat{x}, t) - p[H(\hat{x}, t)], \tag{14}$$

where $H(\hat{x}, t)$ is the local sand height at $x = \hat{x}$ as a function of time and $p[H(\hat{x}, t)]$ is the polynomial fitting of the time-history of the local sand bed height in a least-squares sense.

Similarly, the sand bed height fluctuation along the streamwise direction at $t = \hat{t}$, $H'(x, \hat{t})$, is also extracted using the following equation:

$$H'(x, \hat{t}) = H(x, \hat{t}) - p[H(x, \hat{t})], \tag{15}$$

where $H(x, \hat{t})$ is the sand height profile along the streamwise direction at $t = \hat{t}$ and $p[H(x, \hat{t})]$ is the polynomial fitting of the sand bed height profile.

Based on the sand height fluctuation along the streamwise direction, i.e., $H'(x, \hat{t})$, the surface-normal dimension of the sand wave/ripple patterns, i.e., mean amplitude, is characterized by the rms fluctuation of the sand bed height, σ_H, which is defined as

$$\sigma_H^2(\hat{t}) = \langle H(x, \hat{t}) \cdot H(x, \hat{t}) \rangle_x. \tag{16}$$

Since the wavelength of the sand surface pattern varies significantly along the streamwise direction during the sand wave/ripple formation process, the predominant wavelength of the sand surface patterns cannot be simply extracted by applying the instantaneous two-point correlation of the streamwise sand height fluctuation as given by Kidanemariam and Uhlmann.[62] Instead, the variation of the wave number of the sand surface waves/ripples is evaluated by applying the wavelet analysis of the streamwise sand height fluctuation. In addition, the temporal frequency of the sand surface wave/ripple propagation is also extracted by performing the wavelet analysis of the sand height fluctuations in the time-series.

IV. CHARACTERIZATION OF BOUNDARY LAYER AIRFLOW OVER THE SAND BED SURFACE

Based on the estimation of the threshold shear velocity and corresponding freestream velocity to initiate saltation, i.e., $U_{\infty,th}$ = 5 m/s to $U_{\infty,th}$ = 7.1 m/s, the test freestream airflow velocity is selected to be U_∞ = 8.0 m/s in the present study. The characteristics of the oncoming boundary layer airflow over the smooth bed were measured by using a hot-wire anemometer at a sampling frequency of 5.0 kHz. The time-averaged velocity profiles were calculated based on the velocity data acquired in a period of 5.0 s, i.e., 25 000 samples.

Figure 5 shows the time-averaged velocity profiles of the boundary layer airflow at different streamwise locations along the centerline of the smooth bed surface (i.e., with no sand particles loaded on the bed surface) to reveal the transition process of the boundary layer airflow over the sand bed surface. In the plot, while the velocity data were normalized by the interfacial shear velocity at the smooth bed surface, i.e., $U_+ = U/u_*$, where $u_* = \sqrt{\tau_w/\rho_a} = \sqrt{(\mu/\rho_a)\partial u/\partial z_{z=0}}$, the distance away from the bed surface, z, was normalized by the wall unit, i.e., $z_+ = z/(v/u_*)$. As clearly shown in Fig. 5, the velocity profile at the streamwise location of X = 420 mm is a typical Blasius profile, indicating a laminar boundary layer at the location of X = 420 mm. As the boundary layer airflow develops,
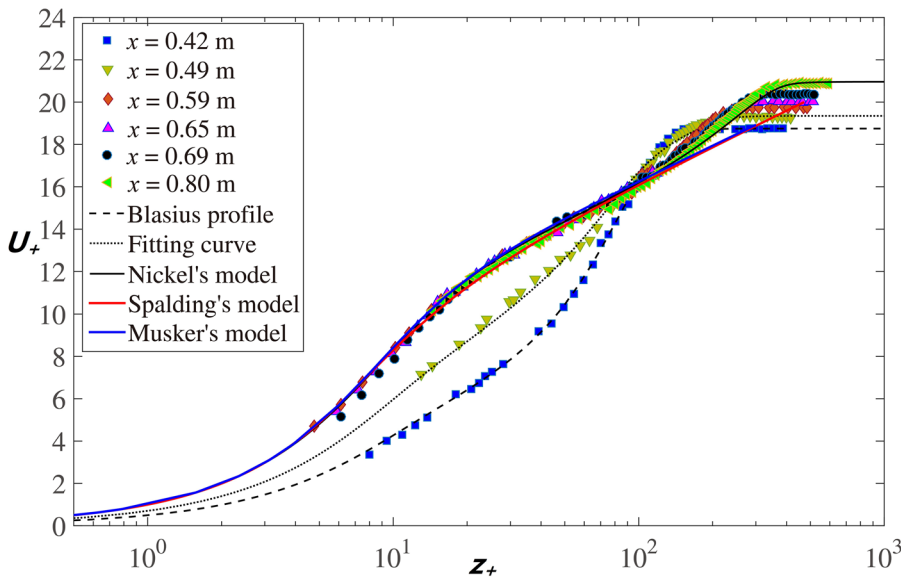
FIG. 5. Time-averaged boundary layer velocity profiles at the different streamwise locations over the smooth sand bed surface at U_∞ = 8.0 m/s. Fitting curves using models of Musker,[64] Spalding,[65] and Nickels.[66]

i.e., at the downstream location of X = 490 mm, the velocity distribution is no longer in the Blasius profile, but with transitional features as discussed by Shahinfar and Fransson.[63] At further downstream locations, i.e., from X = 590 mm to X = 800 mm, the velocity profiles of the boundary layer flow are found to become stable and overlapped with each other. The classical profile models[64–66] of turbulent boundary layers are also plotted in the figure for comparison. It is clearly seen that the velocity profiles at the downstream locations after X = 590 mm follow a log-law and are well fitted with the classical models, indicating a turbulent boundary layer airflow over the surface of the sand bed after the downstream location of X = 590 mm. Since the current study is particularly focused on the sand wave/ripple formation in turbulent flows, the region of interest for the DIP and PTV/PIV measurements is selected to be located in a fully developed turbulent boundary layer airflow (i.e., from X = 875 mm to X = 1255 mm).

Figure 6 shows both the mean velocity profiles and the velocity fluctuations of the gas-phase flow in the boundary layer over the erodible sand bed. It is clearly seen that the gas velocity profiles over the sand bed have a linear dependence on the surface-normal height. Based on the mean velocity profiles, the gas velocity gradient in the boundary layer, $\partial U/\partial z$, is derived (i.e., the linear slope constant of the boundary layer profile). The linear constant is then imported into Eq. (7) to calculate the shear velocity at the interface between the sand surface and the turbulent airflow, i.e., $u_* = \sqrt{\tau_w/\rho_a} = \sqrt{(\mu/\rho_a)\,\partial u/\partial z|_{z=0}} \approx 0.12$ m/s. It is found that the actual shear stress at the sand–air interface is very close to the impact threshold, i.e., $u_{*,th}$ = 0.13 m/s, as predicted above. The slightly lower shear velocity derived in the PIV measurements is suggested to be caused by the existence of the saltation layer, which retards the wind speed and modifies the wind profile by the drag of saltating particles.[67]

The velocity fluctuations within the boundary layer over the sand bed are also shown in Fig. 6. It is clearly seen that the velocity fluctuation over the sand bed is very intense with the maximum

variance reaching about 40% of the freestream velocity. As mentioned by Kok and Renno[60] and Niño and Garcia,[10] while the coherent flow structures in the turbulent boundary layer substantially affect the trajectories of the sand particles ejected from the sand bed, the sand particles suspended in the boundary layer flow could dramatically perturb the flow structures due to the production of small eddies in their shedding wakes and more intense flow ejections, which essentially increases the turbulence intensity in the boundary layer airflow.
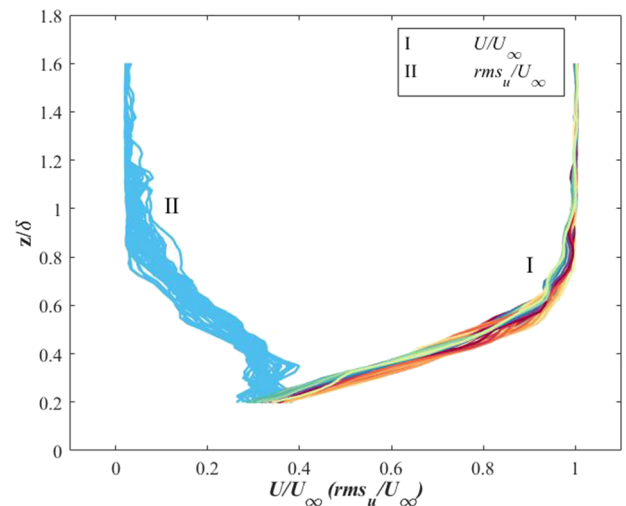

FIG. 6. Mean streamwise velocity profiles in the boundary layer (different colors indicate the repetitive test trials) (I) and velocity fluctuations within the boundary layer (II) over the sand bed surface loaded with sand grains.

V. RESULTS AND DISCUSSION

A. Time-resolved DIP measurements to reveal the dynamic sand bedform evolution process in the turbulent boundary layer airflow

In the present study, a very typical experimental case (i.e., at the freestream airflow velocity of 8.0 m/s, in which the saltation

is sufficiently initiated in the turbulent boundary layer flow) was selected, aiming at revealing the dynamical mechanisms controlling the sand bedform evolution. In order to examine the repeatability of the experiment, multiple trials were conducted under the same test condition. It was found that while discrepancies were observed in the sand surface forms in terms of the starting location of sand wave formation and spacings between sand wave sequences
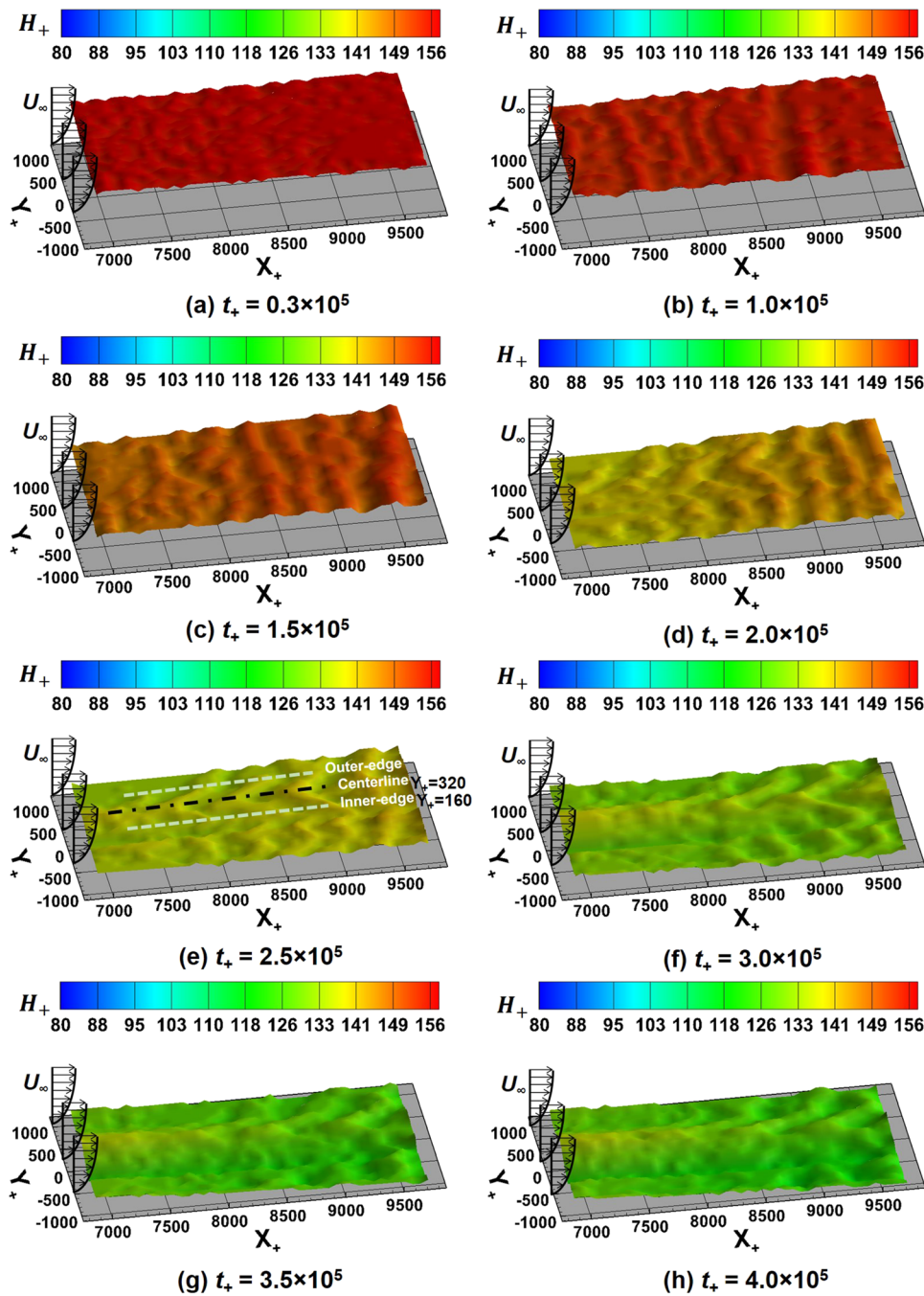

FIG. 7. Time-evolution of the sand surface morphology generated in the turbulent boundary layer airflow with the freestream airflow velocity being U_∞ = 8.0 m/s: (a)–(h) instantaneous sand surface morphology from $t_+ = 0.3 \times 10^5$ to 4.0×10^5.

(suggested to be caused by the uncertain disturbances in upstream), the dominant features of the sand surface morphology were essentially the same [i.e., evolution from two-dimensional (2D) waves to three-dimensional (3D) chevron-shaped ripples].

Figure 7 shows the time-evolution of the sand surface morphology generated at the air/sand interface in the turbulent boundary layer airflow with the freestream airflow velocity being U_∞ = 8.0 m/s. While the streamwise and spanwise coordinates, x and y, and the sand bed height, H, are normalized by the length unit, ν/u_*, the time duration from the beginning of the saltation process, t, is normalized by the time unit, ν/u_*^2,

$$x_+ = \frac{x}{\nu/u_*}; y_+ = \frac{y}{\nu/u_*}, \quad (17)$$

$$H_+ = \frac{H}{\nu/u_*}, \quad (18)$$

$$t_+ = \frac{t}{\nu/u_*^2}. \quad (19)$$

It should be noted that while the spatial and temporal scales of these observations are relatively short in comparison with those realistic sand feature formations in nature, i.e., usually hours or days, it is found that the sand surface features would become very stable after a period in the order of hundreds of seconds. Though further changes in sand surface patterns may occur at the much longer space scales and timescales, we mainly focus on this "early" stage of the sand surface evolution in this paper, as limited by the operational performance of the wind tunnel in terms of the test bed length and operation period.

As can be seen clearly in Fig. 7(a), randomly distributed pits/defects were generated over the sand bed shortly after the wind tunnel was turned on, i.e., at $t_+ = 0.3 \times 10^5$. Such initial sand surface features were also observed by Coleman and Melville[68] and termed as sand wavelets, which were suggested to be formed due to the initial pileup of sand particles and the subsequent roughness growing as more sand particles were trapped by the pileup.[68] It was suggested that the initial 3D sand wavelet lengths are insensitive to the properties of the fluid over the sand bed but principally a function of the properties of the sand particles.[68] As the time goes by, these initial 3D sand wavelets were found to grow and coalesce into the incipient crest lines as shown in Fig. 7(b). During this process, the initially generated random 3D sand wavelet structures were found to be reorganized into 2D wave patterns. Since the amplitude of these 2D wave patterns was relatively small, the flow disturbance is suggested to be linear, with the shear stress having a phase advance against the sand wave structures. As a result, the airflow accelerated upstream of each crest and decelerated downstream, which further increased the amplitude of the wave patterns. Along with the growth of the wave amplitude, the phase advance of the shear stress was found to decrease, resulting in a spatial variation of the shear stress as well as the surface disturbances. As the time goes by, i.e., at $t_+ = 1.5 \times 10^5$, the 2D wave patterns started to break down and develop into complex 3D wave structures (i.e., small sand ripples), first appearing at upstream, as shown in Fig. 7(c). Then, the dispersed 3D sand ripples were found to merge into the larger chevron-shaped sand ripples as they propagated downstream, as shown in Fig. 7(d). It is

suggested that such self-organization behavior of the sand ripples is due to the small fast-moving ripples being absorbed by the larger and slower forms.[16] Based on the similarity between the turbulent flow structures and the surface morphology of the sand ripples,[1,69,70] the sand particle transportation and ripple formation are suggested to be closely coupled with the coherent structures of the turbulent boundary layer airflow, i.e., vortical structures such as reversed horseshoe vortices and quasi-streamwise vortices, with the former being associated with the sweep events and the latter being associated with the ejection events.[71] As the time goes by, while the chevron-shaped sand ripples were found to become more and more evident as shown in Fig. 7(e), the sand surface morphology was stabilized with the streamwise sequences of chevron-shaped ripples being separated by the longitudinal streaks as shown in Fig. 7(f). Secondary currents are suggested to be generated over these surface patterns that further stabilize the sand surface morphology. It should be noted that as more and more sand particles were transported downstream, while the height of the sand bed was found to decrease monotonously (i.e., though the sand particles were found to deposit in downstream locations, the sand grains loaded in the bed were also drifting downstream driven by the airflow without any sand supplement in upstream, causing an erosion of the sand surface as observed in Fig. 7), the surface morphology of the sand bed was kept in a stable shape for an extended period, as shown in Figs. 7(g) and 7(h).

B. Temporal evolution of local sand bed height

Based on the time-resolved DIP measurements of the sand surface morphologies in the turbulent boundary layer airflow as shown in Fig. 7, the sand bed surface was found to evolve from initial random 3D sand wavelets to 2D sand waves and further into well-organized 3D chevron-shaped sand ripples separated by the longitudinal streaks. In order to reveal the time-evolution of the ripple-modulated sand surface morphologies more clearly and
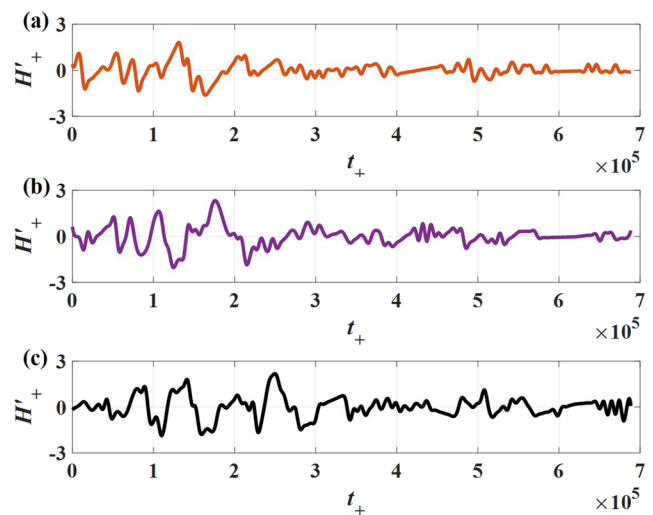

FIG. 8. Time-series of the ripple-modulated sand bed height fluctuations at different streamwise locations along the centerline of the chevron-shaped sand ripple sequence: (a) x_+ = 7000, (b) x_+ = 8250, and (c) x_+ = 9500.

quantitatively, the time-histories of the local sand height variation at three typical streamwise locations (i.e., $x_+ = 7000$, $x_+ = 8250$, and $x_+ = 9500$) were extracted from the DIP measurement results. It is worth mentioning that due to the 3D nature of the chevron-shaped sand ripples with a symmetrical outline, the temporal variations of the local sand height at the different streamwise locations were extracted along both the centerline and one of the side edges (i.e., inner edge) of the chevron-shaped sand ripple sequence as indicated in Fig. 7(e), i.e., the centerline of the sand ripple sequence is located at $y_+ = 320$, and the inner edge of the sand ripple sequence is located at $y_+ = 160$. While the local sand bed height, $H(t)$, can be easily extracted from the DIP measurement results given in Fig. 7, the time-series of the local sand height fluctuations, $H'(t)$, are derived using Eq. (14).

Figure 8 shows the time-series of the local sand bed height fluctuations at the different streamwise locations along the centerline of the chevron-shaped sand ripple sequence (i.e., $y_+ = 320$). Based on the sand surface morphologies given in Fig. 7, it was found that the sand ripples were formed progressively from the upstream to the downstream as the time goes by. Once the stable chevron-shaped sand ripple structures were formed, the local sand bed height would only change slightly due to the fully developed air–sediment flow system over the ripple-modulated sand bed surface. For instance, at the upstream location of $x_+ = 7000$, while the local sand bed height was found to vary dramatically from $t_+ = 0$ to $t_+ = 1.5 \times 10^5$, the amplitude of the sand height fluctuation became much smaller after $t_+ = 2 \times 10^5$ as shown in Fig. 8(a). Similar trends of the sand bed height fluctuations were also observed at the downstream locations,
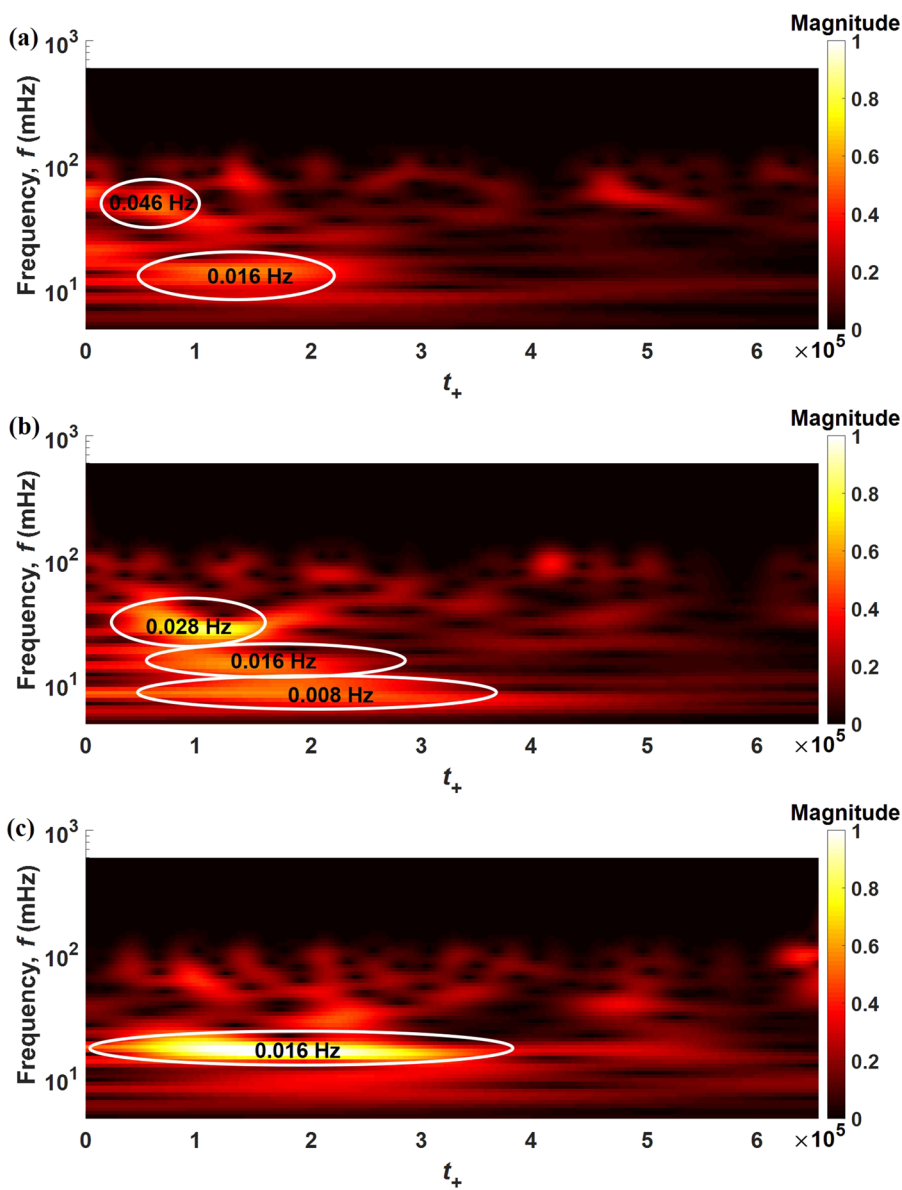

FIG. 9. Continuous wavelet transform (computed in the $L1$ norm) of the time-series of the sand bed height fluctuations at different streamwise locations along the centerline of the chevron-shaped sand ripple sequence: (a) $x_+ = 7000$, (b) $x_+ = 8250$, and (c) $x_+ = 9500$.

i.e., $x_+ = 8250$ and $x_+ = 9500$, with the sand bed height fluctuating significantly at the beginning stage of the sand wave/ripple formation process and becoming stable with very small fluctuations after about $t_+ = 2 \times 10^5$ and $t_+ = 3 \times 10^5$, respectively, as shown in Figs. 8(b) and 8(c).

Since the local sand bed height was found to fluctuate significantly in the time scale with changing amplitudes and frequencies, continuous wavelet transform (i.e., CWT) was implemented in the present study to reveal the frequency content of the sand bed height fluctuations at the different streamwise locations during the transient sand wave/ripple formation process. The CWT used in this study was obtained using the analytic Morse wavelet[72] and computed in the $L1$ norm. The minimum and maximum scales are determined automatically based on the energy spread of the wavelet in frequency and time. Figure 9 shows the wavelet transform of the time-series of the sand bed height fluctuations at the different streamwise locations along the centerline of the chevron-shaped sand ripple sequence: (a) $x_+ = 7000$, (b) $x_+ = 8250$, and (c) $x_+ = 9500$. It is seen that at the upstream location of $x_+ = 7000$, while a frequency of $f = 0.046$ Hz is observed at the beginning of the sand wave formation process, it disappears quickly after $t_+ = 1 \times 10^5$. Along with the vanishing of this "high" frequency wave component (i.e., it is suggested to be the initial 3D wavelet component), a lower frequency of $f = 0.016$ Hz becomes dominant as a result of the 2D wave formation over the sand bed surface. Since the amplitude of the sand height fluctuation was found to become very small as the time goes by, the frequency component of $f = 0.016$ vanishes after $t_+ = 2 \times 10^5$ as can be seen clearly in Fig. 9(a). At the location of $x_+ = 8250$, similar to that observed at the upstream location, a frequency component of $f = 0.028$ Hz is found to dominate at the beginning of the sand wave formation process, which vanishes quickly after $t_+ = 1.5 \times 10^5$. Meanwhile, lower frequency components (i.e., $f = 0.016$ Hz and $f = 0.008$ Hz) are found to appear as shown in Fig. 9(b), corresponding to the development of 2D waves over the sand bed surface. At the location of $x_+ = 9500$, since the 2D waves were found to persist longer, a dominant frequency of $f = 0.016$ Hz is clearly seen in Fig. 9(c), which vanishes after $t_+ = 3.5 \times 10^5$. The vanishing of the dominant frequency components indicates a steady sand wave pattern being formed along the centerline of the chevron-shaped sand ripple sequence.

Figure 10 shows the time-histories of the sand bed height fluctuations at the different streamwise locations (i.e., $x_+ = 7000$, $x_+ = 8250$, and $x_+ = 9500$) along the inner edge of the chevron-shaped sand ripple sequence (i.e., $y_+ = 160$). It was found that although the wave structures were generated over the entire measurement region as shown in Fig. 6, the sand bed height fluctuation at the upstream location, $x_+ = 7000$, was relatively small throughout the sand ripple formation and development process as shown in Fig. 10(a). As the sand ripples propagated downstream, the local sand bed height fluctuation was found to become more and more evident, i.e., $x_+ = 8250$ and $x_+ = 9500$, as shown in Figs. 10(b) and 10(c). Similar to that along the centerline of the chevron-shaped sand ripple sequence, the sand bed height fluctuation along the ripple edge was also found to be more intense at the early stage of the sand ripple formation process and become weaker when the sand ripple patterns were stabilized.

The wavelet transforms of the time-series of the sand bed height fluctuations at the different streamwise locations along the inner
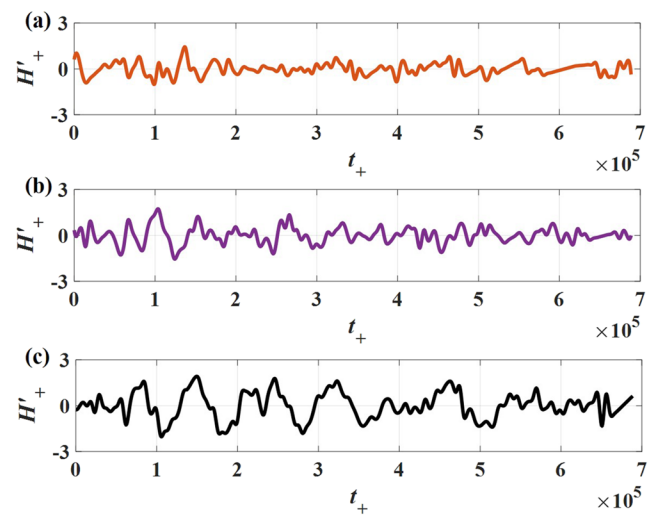

FIG. 10. Time-series of the ripple-modulated sand bed height fluctuations at different streamwise locations along the inner edge of the chevron-shaped sand ripple sequence: (a) $x_+ = 7000$, (b) $x_+ = 8250$, and (c) $x_+ = 9500$.

edge of the chevron-shaped sand ripple sequence are shown in Fig. 11. For the sand bed height fluctuation at the upstream location, i.e., $x_+ = 7000$, the energy is mainly concentrated at the frequency of $f = 0.035$ Hz at the beginning of the sand wave formation, which vanishes after $t_+ = 1.5 \times 10^5$ as shown in Fig. 11(a). At the location of $x_+ = 8250$, while a similar "high" frequency component of $f = 0.035$ Hz is observed at the beginning stage, it shifts to $f = 0.016$ Hz as clearly shown in Fig. 11(b), which corresponds to the formation of the well-structured waves/ripples. While the surface patterns become stable, the frequency component vanishes. At the location of $x_+ = 9500$, along with the formation of 2D waves and 3D ripples, the energy is found to concentrate in a narrow band with frequency components ranging from $f = 0.011$ Hz to $f = 0.016$ Hz as clearly seen in Fig. 11(c), which vanishes after $t_+ = 4.5 \times 10^5$. It is suggested that the formation of the chevron-shaped sand ripples is essentially due to the discrepancy of the local sand wave propagation (as indicated by the varying frequency components) in different transverse locations caused by the asymmetric nature and instability of the turbulent boundary layer airflow.[73]

C. Spatial variations of the ripple-modulated sand surface along streamwise directions

To further evaluate the sand ripple/wave characteristics formed in the turbulent boundary layer airflow, the spatial variations of the ripple-modulated sand surface along the streamwise directions were also extracted along both the centerline and the inner edge of the chevron-shaped sand ripple sequence (i.e., the centerline of the sand ripple sequence at $y_+ = 320$ and the inner edge of the sand ripple sequence at $y_+ = 160$) at three typical time instants, i.e., (1) at $t_+ = 1 \times 10^5$ when the 2D sand waves dominated in the measurement region, (2) at $t_+ = 2 \times 10^5$ when the 3D chevron-shaped sand ripples were formed at upstream, and (3) at $t_+ = 4 \times 10^5$ when the sand ripple structures were fully developed and stabilized over the
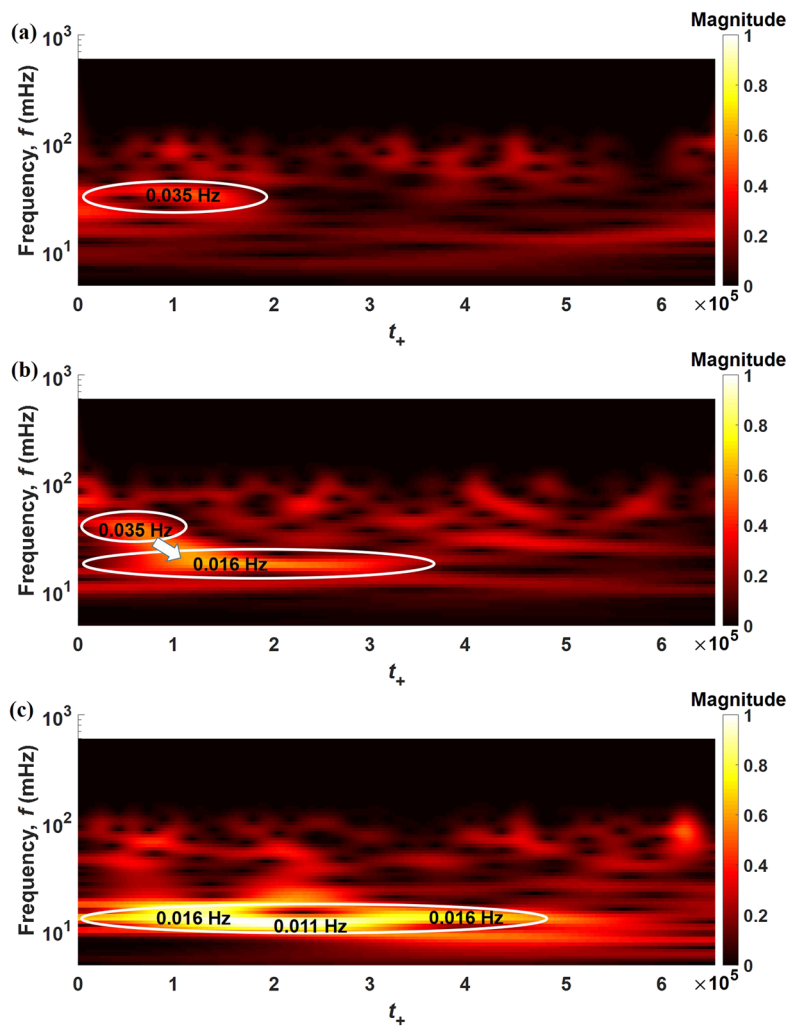
FIG. 11. Continuous wavelet transform (computed in the $L1$ norm) of the time-series of the sand bed height fluctuations at different streamwise locations along the inner edge of the chevron-shaped sand ripple sequence: (a) $x_+ = 7000$, (b) $x_+ = 8250$, and (c) $x_+ = 9500$.

sand bed. Then, the sand bed height fluctuation profiles along the streamwise direction, $H'(x)$, are extracted using Eq. (15).

Figure 12 shows the fluctuation profiles of the sand bed surface along the centerline of the chevron-shaped sand ripples (i.e., $y_+ = 320$) at the three selected time instants (i.e., $t_+ = 1 \times 10^5$, $t_+ = 2 \times 10^5$, and $t_+ = 4 \times 10^5$). The corresponding wavelet transforms of the sand surface profiles are given in Fig. 13. As can be seen clearly in Fig. 12(a), at the time instant of $t_+ = 1 \times 10^5$, the streamwise sand surface fluctuation profile shows a clear waveform, which is due to the sand surface morphology being almost two-dimensional at the early stage of sand wave/ripple formation. By performing the wavelet transform of the waveform, it is found that in upstream from $x_+ = 7000$ to $x_+ = 8000$, the energy is mainly dominated in two wave components with the wave numbers of $k = 0.18$ rad/mm ($k = 2\pi/\lambda$, where λ is the wavelength) and $k = 0.12$ rad/mm being identified as shown in Fig. 13(a). As the wave structures develop to downstream, though the wave number varies, the waveforms are found to be very prominent when the 2D waves are formed over the sand bed surface. As the time goes by, i.e., $t_+ = 2 \times 10^5$, the sand surface morphology was found to become more three-dimensional, starting from
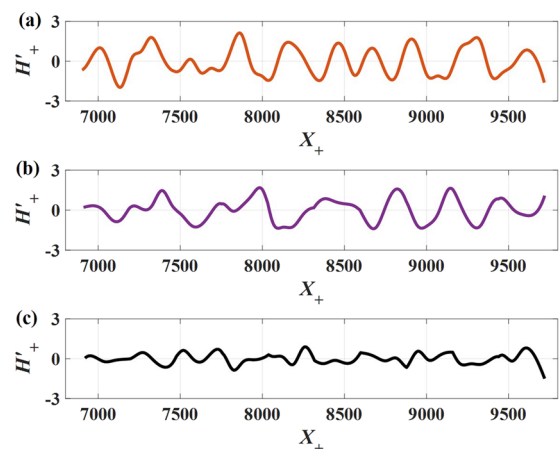

FIG. 12. Spatial fluctuation profiles of the sand bed surface along the centerline of the chevron-shaped sand ripple sequence: (a) $t_+ = 1 \times 10^5$, (b) $t_+ = 2 \times 10^5$, and (c) $t_+ = 4 \times 10^5$.

FIG. 13. Continuous wavelet transform (computed in the $L1$ norm) of the spatial fluctuation profiles of the sand bed surface along the centerline of the chevron-shaped sand ripple sequence: (a) $t_+ = 1 \times 10^5$, (b) $t_+ = 2 \times 10^5$, and (c) $t_+ = 4 \times 10^5$.
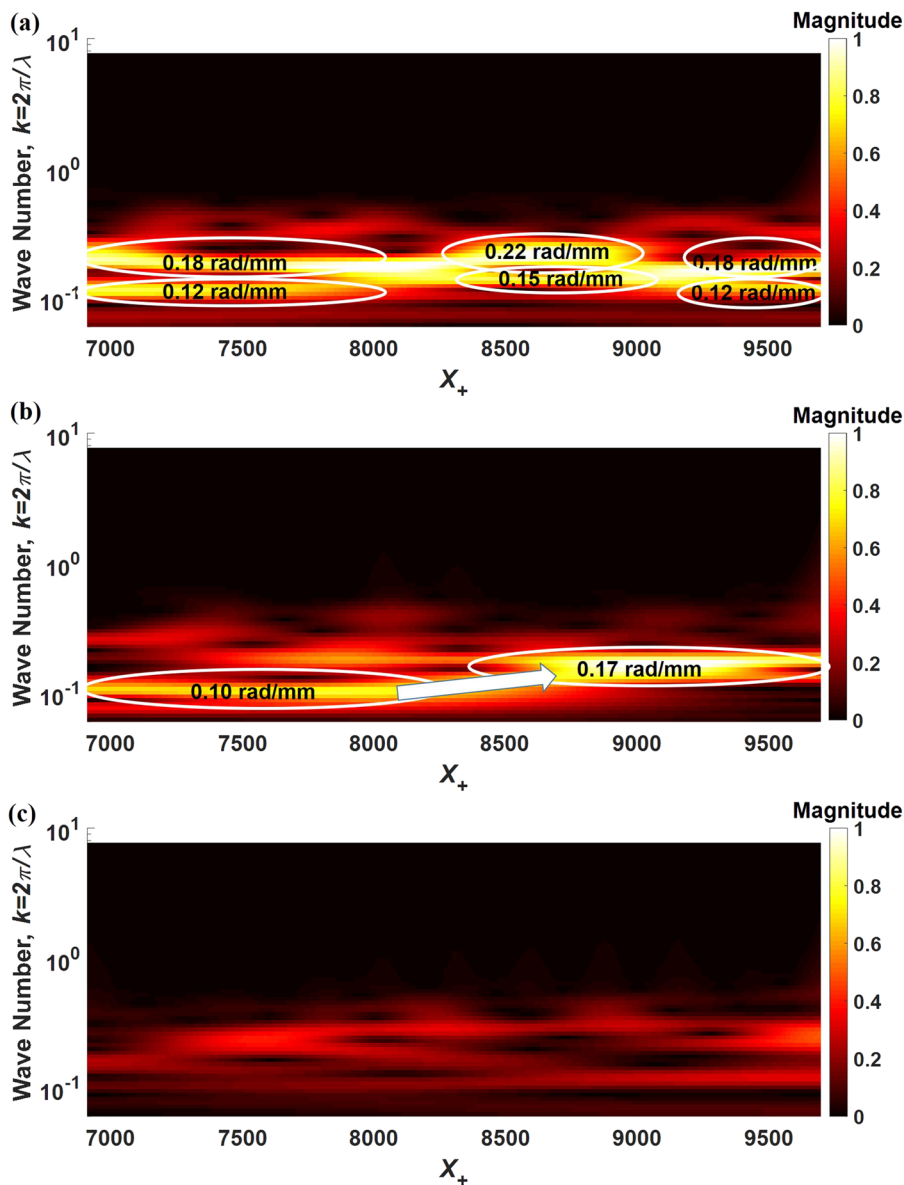
the upstream as already revealed in Fig. 7. Along with the evolution of the surface morphology, the fluctuating magnitude of the sand surface waveform is found to become smaller, with the wavelength at upstream becoming longer, while the wavelength at downstream remaining almost unchanged as shown in Fig. 12(b). Based on the wavelet transform of the sand surface profile as shown in Fig. 13(b), a clear transition of the dominant wave number from $k = 0.10$ rad/mm to $k = 0.17$ rad/mm is observed, indicating a combination of two wavelengths of the surface profile at this transient moment, i.e., the upstream 3D sand ripple of $\lambda_+ = 497$ and the downstream 2D sand wave of $\lambda_+ = 293$. As the surface morphology became stable, i.e., $t_+ = 4 \times 10^5$, the sand surface fluctuation amplitude is found to become smaller as shown in Fig. 12(c). Based on the wavelet transform as

given in Fig. 13(c), it is found that the energy dominated by the wave structures becomes very small as the 3D sand ripple structures were fully developed and became stable along the sand ripple centerline. It should be noted that the wavelength measured in the present study agrees well with those scaled data, i.e., λ/d as a function of d/z_0, where d is the sand grain size and z_0 is estimated to be $z_0 = 0.03–0.1d$, as given by Charru et al.[1]

Figure 14 shows the spatial fluctuation profiles of the sand bed surface along the inner edge of the chevron-shaped sand ripple sequence (i.e., $y_+ = 160$) at the three selected time instants (i.e., $t_+ = 1 \times 10^5$, $t_+ = 2 \times 10^5$, and $t_+ = 4 \times 10^5$). Similar to that along the sand ripple sequence centerline, the sand surface profile along the inner edge of the sand ripple sequence also shows a clear
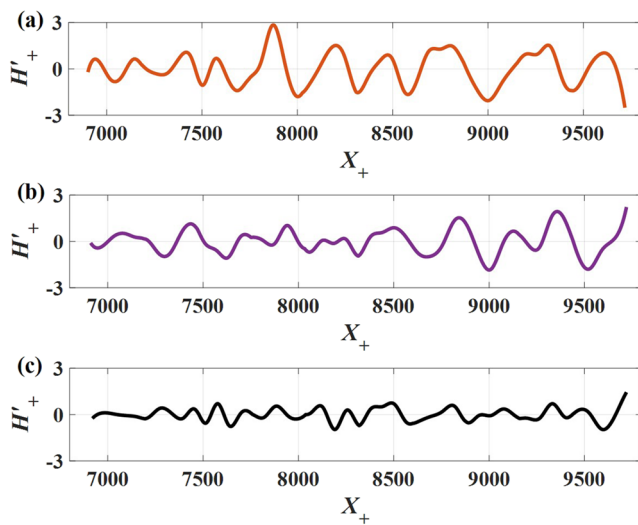
FIG. 14. Spatial fluctuation profiles of the sand bed surface along the inner edge of the chevron-shaped sand ripple sequence: (a) $t_+ = 1 \times 10^5$, (b) $t_+ = 2 \times 10^5$, and (c) $t_+ = 4 \times 10^5$.

periodic waveform at the early stage of sand wave/ripple formation, i.e., $t_+ = 1 \times 10^5$, with the wavelength being almost constant as shown in Fig. 14(a). Based on the wavelet transform, a dominant wave number of $k = 0.17$ rad/mm is extracted, which then develops to $k = 0.10$ rad/mm in downstream as shown in Fig. 15(a), which is very similar to that along the sand ripple centerline due to the 2D nature of the sand surface morphology at $t_+ = 1 \times 10^5$. As the time goes by, i.e., $t_+ = 2 \times 10^5$, along with the transition of the sand surface morphology from the 2D waves to the 3D ripples, while the wave structures at the upstream locations are found to become flattened, the wavelength in the downstream region is kept unchanged as shown in Fig. 14(b). The wavelet transform of the sand surface profile given in Fig. 15(b) reveals that the wave/ripple features are also dominated by two wave numbers, i.e., $k = 0.17$ rad/mm and $k = 0.10$ rad/mm, which essentially shows a spatial lag (the sand surface morphology becomes three-dimensional) in comparison with that along the centerline of the sand ripple sequence. As the surface morphology became stable, i.e., $t_+ = 4 \times 10^5$, the sand surface profile is found to become flattened with only small fluctuations as shown in Fig. 14(c). It is suggested that the flattening of the surface profile is due to the formation of the streamwise streaks over the sand bed as can be observed in Figs. 7(e)–7(h). Correspondingly, the energy becomes very small in the wavelet transform of the surface profile as given in Fig. 15(c).

Based on the sand surface fluctuation profiles along the centerline (i.e., $y_+ = 320$) and the inner edge (i.e., $y_+ = 160$) of the chevron-shaped sand ripple sequence as given in Figs. 12 and 14, the surface-normal dimension of the sand wave/ripple patterns, i.e., mean amplitude, σ_H, can be characterized by the root-mean-square (rms) of the sand bed height fluctuation using Eq. (16). Thus, the time-evolution of the sand surface fluctuation amplitude can be derived by applying the algorism throughout the entire sand

wave/ripple formation process. Figure 16 shows the time-evolutions of the sand surface fluctuation amplitude along the centerline (i.e., $y_+ = 320$) and the inner edge (i.e., $y_+ = 160$) of the chevron-shaped sand ripple sequence. It is clearly seen that right after the saltation was initiated, the fluctuation amplitude of the sand bed surface increases quickly due to the formation of the initial random 3D sand wavelets and the 2D wave development in the early stage of the sand wave/ripple evolution process, i.e., from $t_+ = 0$ to $t_+ = 1.2 \times 10^5$. As revealed by Bagnold,[6] owing to the time-lag between the changes in the rate of sand-flow and resulting changes in the airflow velocity, there are upstream removal and downstream deposition of the sand particles during the sand wave/ripple formation, thus leading to the rapid increase in the sand surface fluctuation amplitude. As the time goes by, while the 2D sand waves were developed into the well-organized 3D chevron-shaped sand ripples as a result of the spatial variation of shear stress as well as the surface disturbances within each trough and crest of the sand waves,[1] the sand surface fluctuation amplitude was found to decrease monotonously from $t_+ = 1.2 \times 10^5$ to $t_+ = 4 \times 10^5$. It is suggested that the decrease in the sand wave/ripple amplitude is essentially due to the intense transverse component of the shear flow as the 3D surface features were formed. Once the ripple-modulated sand surface morphology was stabilized after $t_+ = 4 \times 10^5$, the sand surface fluctuation amplitude was found to be almost not changed with a mean value of about $\bar{\sigma}_{H_+} = 0.5$. It should be noted that while there exists a phase lag between the sand surface waveforms along the centerline and the inner edge of the sand ripple sequence, the fluctuating amplitude of the two sand wave patterns is found to change concurrently throughout the sand wave/ripple formation process.

D. Ensemble-averaged gas-phase flow statistics in the air–sediment flow system over the erodible sand bed before and after the sand wave/ripple formation

As the sand bedform evolves driven by the turbulent boundary layer airflow, the air–sediment flow structures would also be altered along with the formation of the sand wave/ripple morphologies. In the present study, in order to evaluate the effects of the evolving sand bedform on the two-phase (i.e., air–sediment) flow structures over the erodible sand bed, a series of PIV/PTV measurements were also conducted, with the measurement plane being located perpendicularly along the centerline of the sand ripple sequence, i.e., $y_+ = 320$. It is worth mentioning that the size of the field of view (FOV) in the PIV + PTV measurements was selected based on the measured wavelength of the sand waves (at least to cover a complete waveform for the further correlation) while maximizing the measurement resolution (i.e., the smaller the FOV, the higher the measurement resolution). Based on the PIV measurement results processed with the oil droplet tracer images, the ensemble-averaged gas-phase flow statistics (i.e., mean velocity, vorticity, Reynolds stress, and TKE) were first derived both before and after the sand wave/ripple formation. As mentioned above, at the very initial stage of the sand surface morphology evolution, i.e., $t_+ = 0$ to $t_+ = 0.5 \times 10^5$, there were only randomly distributed pits/defects being generated over the sand bed due to the initial pileup of sand particles. The gas-flow structures in this period are suggested to be greatly affected by the sand particles ejected from the
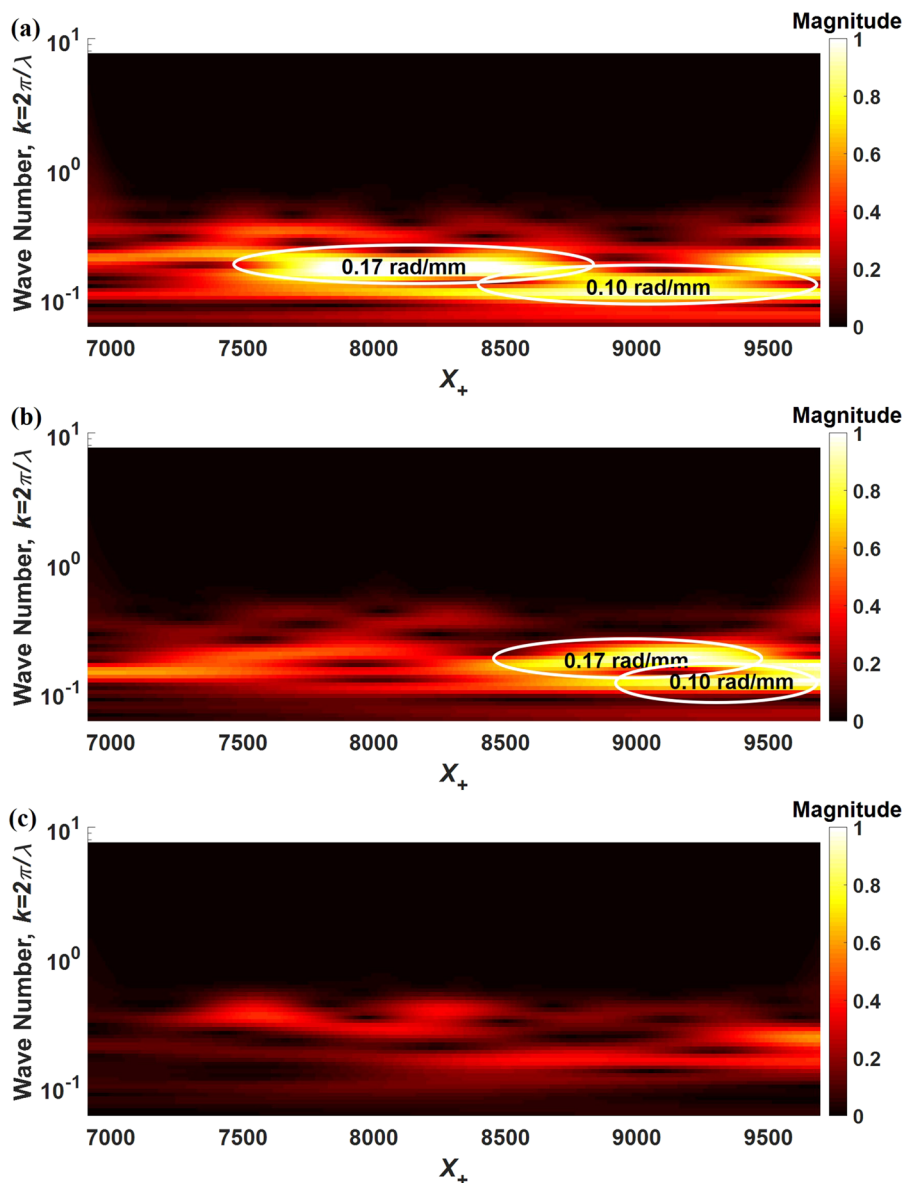
FIG. 15. Continuous wavelet transform (computed in the $L1$ norm) of the spatial fluctuation profiles of the sand bed surface along the inner edge of the chevron-shaped sand ripple sequence: (a) $t_+ = 1 \times 10^5$, (b) $t_+ = 2 \times 10^5$, and (c) $t_+ = 4 \times 10^5$.

sand bed[55] but have a minimal modification by the sand bedform. As the sand wave/ripple structures were sufficiently developed, i.e., $t_+ = 2.0 \times 10^5$ to $t_+ = 2.5 \times 10^5$, while the gas-flow structures were still under strong interactions with the sand particles suspended in the airflow, they would also be significantly modified by the wavy sand bedforms as suggested by Charru *et al.*[1]

Figure 17 shows the contours of the ensemble-averaged gas-phase flow statistics in the air–sediment flow system over the erodible sand bed before and after the sand wave/ripple formation. More specifically, "before the sand wave/ripple formation" refers to the very initial stage, i.e., $t_+ = 0–0.5 \times 10^5$, and "after the sand wave/ripple formation" refers to the period when the sand wave/ripple structures are sufficiently developed, i.e., $t_+ = 2.0 \times 10^5$

to 2.5×10^5. The nondimensional time-averaged flow velocity fields are illustrated in Figs. 17(a) and 17(e). It is clearly seen that after the sand ripple structures are formed, the airflow boundary layer is thickened as indicated by the larger area of velocity defect. As revealed by Charru *et al.*,[1] there is a linear response of the shear stress and the presence of larger slopes of sand waves. Therefore, the formation of the sand wave/ripple structures in this study is suggested to induce an increase in shear stress at the air/sand interface. The increased shear stress would generate more intense flow injection events, which tends to increase the frequency of occurrence of wall ejections for sand particles.[10] As suggested by Zhu *et al.*,[55] the ejected sand particles would have a non-negligible energy/momentum exchange with the gas phase, which would result
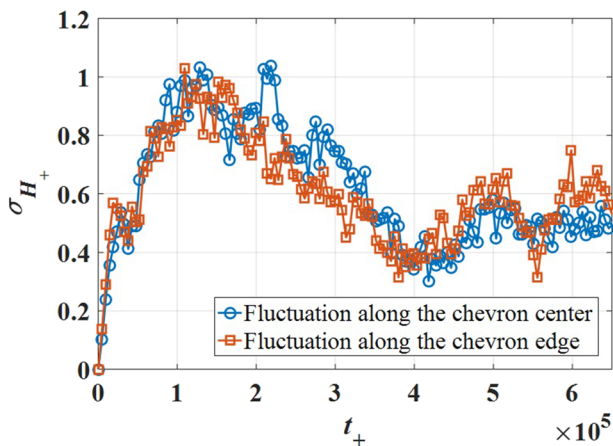
FIG. 16. Time-evolution of the sand surface fluctuation amplitude along the centerline (i.e., y_+ = 320) and the inner edge (i.e., y_+ = 160) of the chevron-shaped sand ripple sequence.

in the sublayer flow deceleration and thickening of the airflow boundary layer.

Figures 17(b) and 17(f) depict the nondimensional time-averaged vorticity (i.e., $\bar{\omega} \nu / u_*^2$, where $\bar{\omega}$ is the time-averaged vorticity given by $\partial \bar{u} / \partial z - \partial \bar{v} / \partial x$) fields before and after the sand wave/ripple formation. It is known that shear layers could be formed by the flow separation from the crest of sand waves/ripples. These shear layers would involve vortices owing to the Kelvin–Helmholtz (K–H) instabilities.[33] Along with the development of the sand waves/ripples, more vortical structures are suggested to be formed in the air–sediment flow system, which could essentially induce a stronger fluid mixing and higher shear stress on the lee-side of the sand waves/ripples. While propagating over the following stoss-side of sand waves/ripples, these vortical structures would extend toward the free surface as indicated by the lifted vortices shown in Fig. 17(f). Meanwhile, owing to the enhanced fluid mixing along with the sand wave/ripple formation, an increase in Reynolds stress (i.e., $-\overline{u'v'}/u_*^2$, where u' and v' are the fluctuations of u and v) and enhancement of turbulence production [as indicated by the TKE, i.e., $(\overline{u'^2} + \overline{v'^2})/2u_*^2$] are also observed as clearly shown in Figs. 17(c) and 17(g) and Fig. 17(d) and 17(h).

E. Surface-normal velocity field of the airborne sand particles over the wave/ripple-modulated sand surface

In order to reveal the interactions between the dynamically evolving sand wave/ripple structures and the sand particle flow patterns in the near-bed flow field, the velocity field of the sand particles was also derived based on the PTV/PIV measurements. It should be noted that while both the horizontal and vertical velocity components, i.e., u and v, of the sand particles were calculated in the present study, only the vertical velocity component, i.e., surface-normal velocity, was presented in this paper to illustrate the vertical behaviors of the airborne sand particles and their interactions with the dynamically evolving sand bed morphology. As mentioned

above, the surface-normal velocity of the sand particles is normalized by the velocity unit, i.e., the measured shear velocity at the interface between the sand surface and the airflow, u_*.

Figure 18 shows the time-evolution of the surface-normal velocity field of the airborne sand particles during the dynamic sand wave/ripple formation process. As can be seen clearly in Fig. 18(a), at the very beginning of the saltation process, i.e., $t_+ = 0.3 \times 10^5$, while a group of sand particles were ejected from the sand bed driven by the turbulent boundary layer airflow, the surface-normal velocities of these sand particles are found to be rather small and random due to the relatively flat sand bed surface. As the time goes by, once the 2D sand waves were formed over the sand bed, i.e., at $t_+ = 1.0 \times 10^5$, the surface-normal velocity field of the sand particles was found to be highly disturbed, featured by the alternating positive and negative velocity regions as shown in Fig. 18(b). It is also found that the surface-normal velocity distribution is well in phase with the sand surface profile, with the maximum positive velocity being always located above the windward slope of the sand waves. As the 2D sand waves break into the small dispersed sand ripples at $t_+ = 1.5 \times 10^5$, the surface-normal velocities of the sand particles are found to become very small but still in phase with the sand surface pattern as shown in Fig. 18(c). The small dispersed sand ripples were then quickly merged into the larger chevron-shaped sand ripples, which are found to have a significant impact on the near-bed flow field as indicated by the recurrent alternating positive and negative velocity regions over the sand bed surface as shown in Fig. 18(d). As the time goes by, while the amplitude of the sand ripples decreases monotonously in the period of $t_+ = 2.0 \times 10^5$ to $t_+ = 3.0 \times 10^5$, the surface-normal velocities of the sand particles are also found to decrease correspondingly as shown in Figs. 18(e) and 18(f). It is worth mentioning that while the surface-normal velocity distribution of the airborne sand particles in the near-bed flow field is in phase with the sand bed surface profile, there exists a phase lag between them, i.e., while the maximum positive surface-normal velocity is located above the windward slope of the sand surface profile, the maximum negative surface-normal velocity is located above the leeward slope of the sand surface profile.

F. Correlation between the wave/ripple-modulated sand surface profile and the sand particle velocity distribution in the near-bed flow field

In order to further reveal the interactions between the near-bed sand flow field and the dynamically evolving sand bed surface morphology, a series of cross-correlations were calculated between the sand bed surface pattern and the surface-normal sand velocity profiles at the different vertical distances away from the sand bed surface, namely, R, which is defined as

$$R(\Delta, \delta_z) = \frac{\langle H'(x) \cdot v'(x + \Delta, \delta_z) \rangle_x}{\sigma_H \cdot \sigma_v(\delta_z)}, \qquad (20)$$

where Δ is the spatial lag and δ_z is the vertical distance away from the sand bed surface,

$$\delta_z = z - z_0(t), \qquad (21)$$

where $z_0(t)$ is the instantaneous coordinate of the local sand bed surface and z is the vertical coordinate of the velocity extraction location.
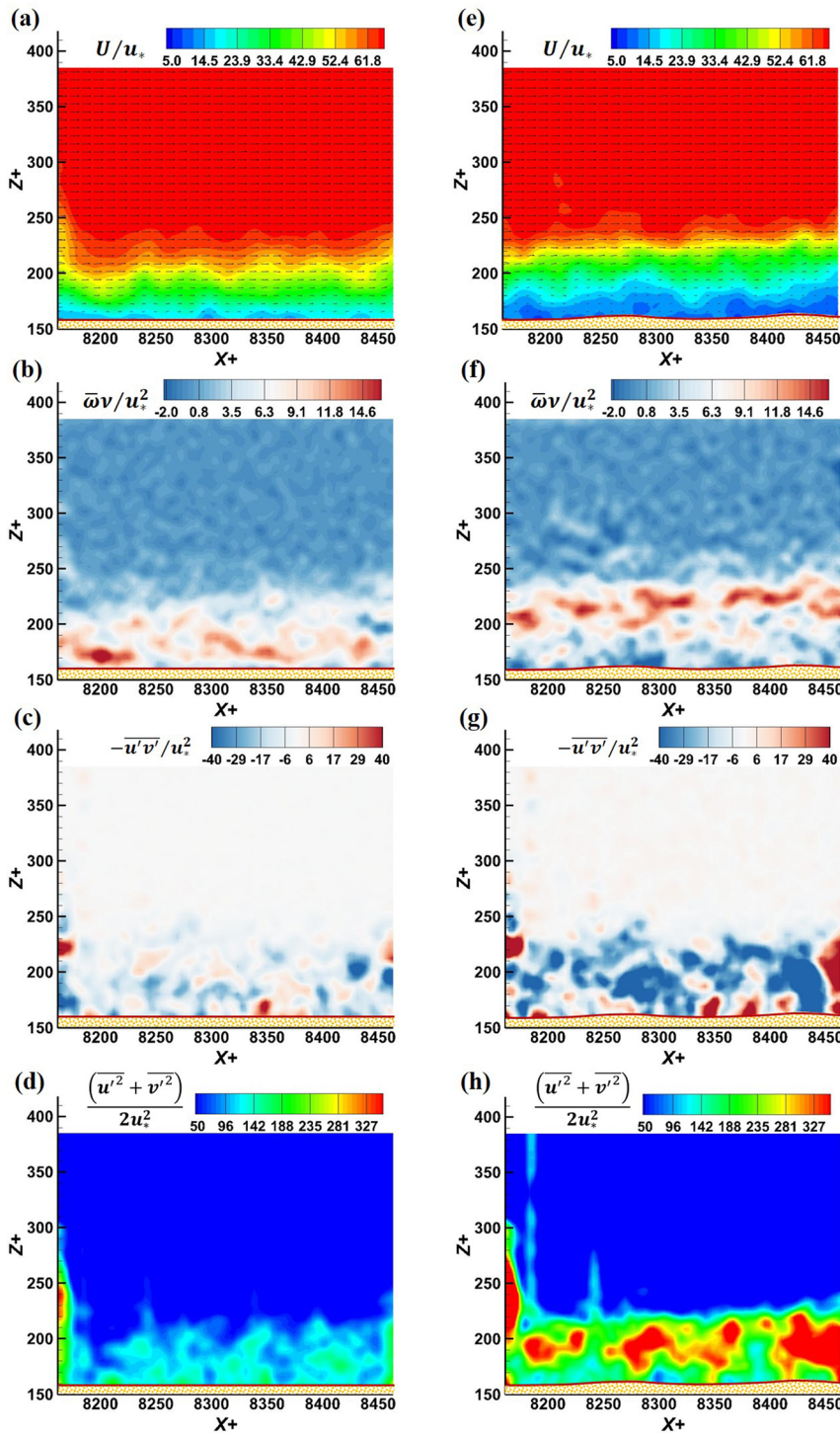
FIG. 17. Contours of ensemble-averaged gas-phase flow statistics in the air–sediment flow system over the erodible sand bed before and after the sand wave/ripple formation. (a)–(d) Before the sand wave/ripple formation, i.e., $t_+ = 0$–0.5×10^5. (e)–(h) After the sand wave/ripple formation, i.e., $t_+ = 2.0 \times 10^5$ to 2.5×10^5.

Figure 19 shows the time-evolution of the cross-correlation curves between the sand bed surface pattern and the surface-normal sand velocity profiles extracted at the different surface-normal distances δ_z. As can be seen clearly in Fig. 19(a), at the beginning of the saltation process, i.e., $t_+ = 0.3 \times 10^5$, since the sand bed surface is rather flat with almost no perturbation extruding into the boundary layer airflow, the surface-normal velocity distribution of the airborne sand particles appears to be irrelevant to the sand
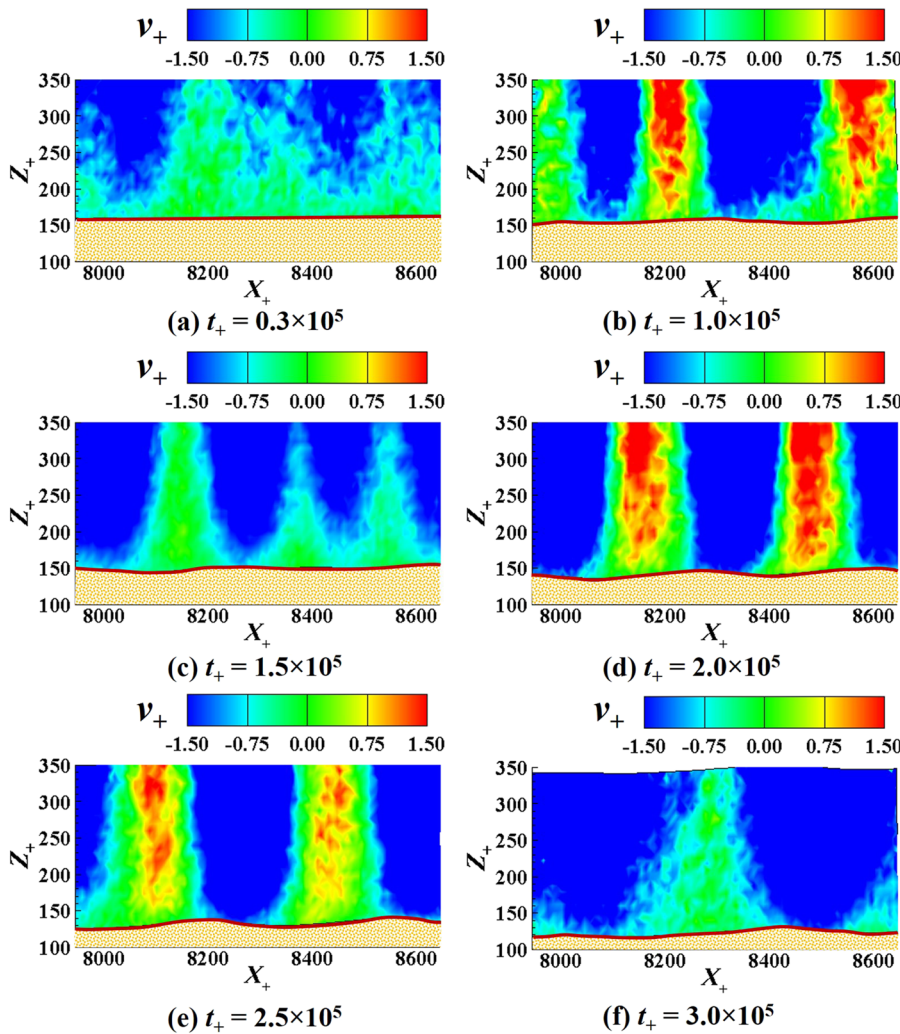
FIG. 18. Time-evolution of the surface-normal velocity field of the airborne sand particles during the sand wave/ripple formation process: (a)–(f) instantaneous surface-normal velocity field of the sand particles from $t_+ = 0.3 \times 10^5$ to 3.0×10^5.

surface profile as indicated by the low random values of R throughout the near-bed flow field. As the time goes by, along with the formation of the 2D sand waves, i.e., at $t_+ = 1.0 \times 10^5$, the surface-normal velocity field of the sand particles was found to be highly correlated with the sand surface profile as clearly shown in Fig. 19(b). While there exists a phase lag between the sand surface profile and the sand velocity distribution, i.e., $\Delta_+ \approx -200$ where $|R|_{max}$ is achieved, the value of $|R|$ appears to be increasing as the surface-normal distance increases from $\delta_{z+} = 50$ to $\delta_{z+} = 200$ and becoming smaller at $\delta_{z+} = 250$. This close correlation between the sand surface profile and the sand velocity distribution is found to be disrupted when the 2D sand waves break into the small dispersed sand ripples at $t_+ = 1.5 \times 10^5$, with the value of $|R|_{max}$ being reduced to only about 0.6 at zero phase lag as shown in Fig. 19(c). Then, along with the formation of the chevron-shaped sand ripples at $t_+ = 2.0 \times 10^5$, the correlation between the sand-ripple modulated surface profile and the sand particle velocity distribution in the near-bed flow field was found to be recovered, with the phase lag being about $\Delta_+ \approx -160$

as shown in Fig. 19(d). Similar to that in the early stage when the 2D sand waves were formed, the value of $|R|$ at this moment is also found to increase at the larger surface-normal distance, i.e., from $\delta_{z+} = 50$ to $\delta_{z+} = 200$, but with a tendency of retraction beyond $\delta_{z+} = 250$. As the time goes by, while the amplitude of the sand ripples decreases monotonously in the period of $t_+ = 2.0 \times 10^5$ to $t_+ = 3.0 \times 10^5$, the value of $|R|_{max}$ is also found to decrease, but with the phase lag being consistent at $\Delta_+ \approx -160$ as shown in Figs. 19(e) and 19(f). It should be noted that the propagation of the sand waves/ripples, i.e., a process of upstream removal and downstream deposition of the sand particles, is essentially caused by the phase lag between the changes in the sand surface profile and the resulting changes in the near-bed flow field.[6] As the sand surface morphology becomes more and more stable (featured by the well-organized 3D chevron-shaped sand ripples separated by the longitudinal streaks), the corresponding phase lag is found to shift back to $\Delta_+ \approx 0$, indicating a concurrent fluctuation pattern for the sand bed surface and the near-bed flow field.
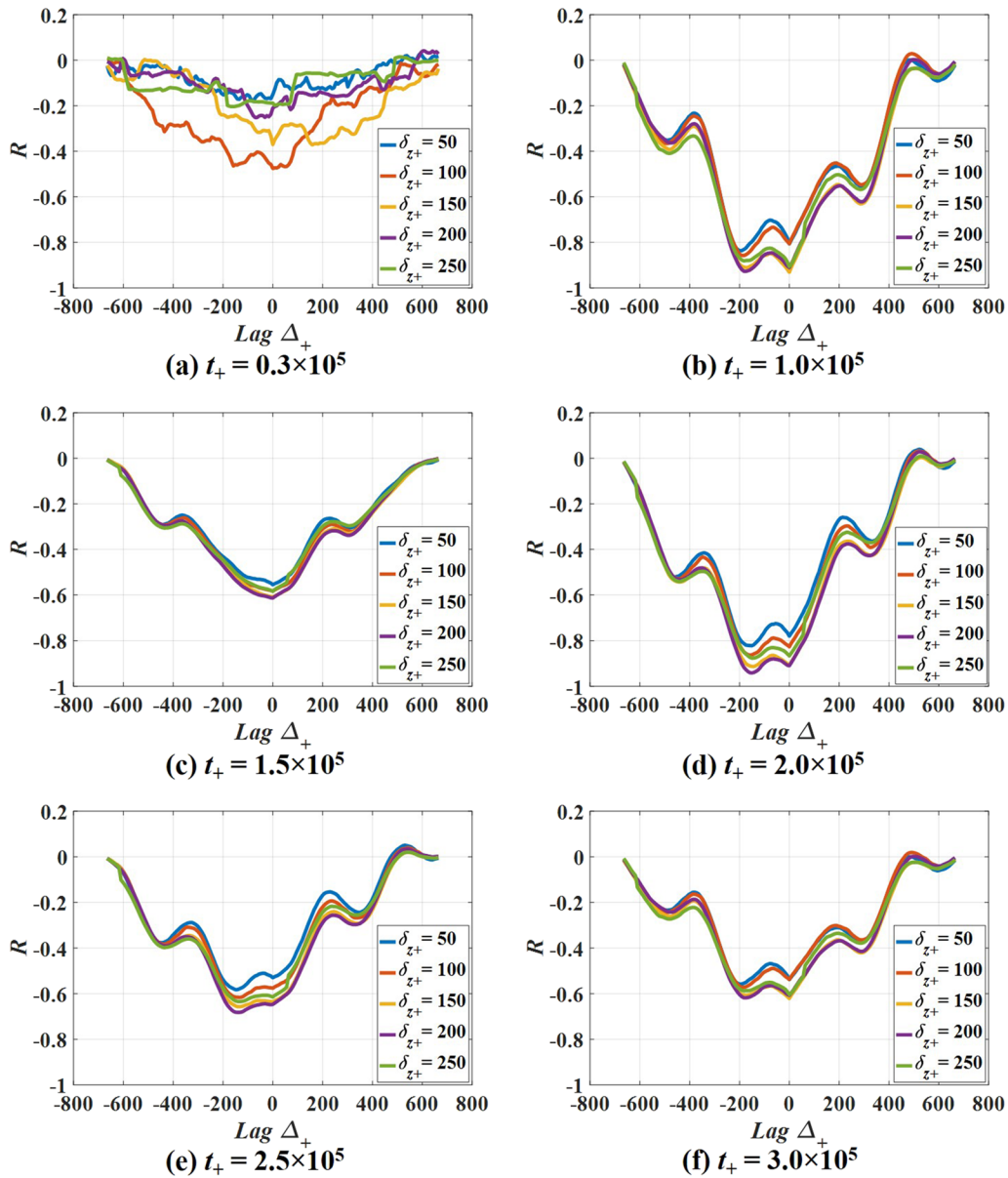
FIG. 19. Time-evolution of the cross-correlation between the sand bed surface pattern and the surface-normal sand velocity profiles: (a)–(f) cross-correlation curves from $t_+ = 0.3 \times 10^5$ to 3.0×10^5.

Based on the data of cross-correlation coefficients between the sand surface profile and the near-bed flow field given in Fig. 19, the time-variations of $|R|_{max}$ at the different surface-normal distances during the dynamic sand wave/ripple formation process are extracted and plotted in Fig. 20. It is clearly seen that the entire sand wave/ripple formation process can be divided into five phases: (I) initial strengthening phase, (II) transition phase, (III) ripple-modulated re-strengthening phase, (IV) stabilizing phase, and (V) longitudinal phase. In the (I) initial strengthening phase, while the

2D sand waves are formed progressively over the sand bed surface, the surface-normal velocity field of the sand particles is changed correspondingly with the alternating positive and negative velocity regions being generated. Along with the increase in the 2D wave amplitude, the correlation between the sand surface profile and the sand flow field is strengthened with a linear increase in $|R|_{max}$. Then, due to the spatial variation of the shear stress and the surface disturbances, the 2D wave patterns break into the dispersed 3D sand ripples, which is called the (II) transition phase. During this
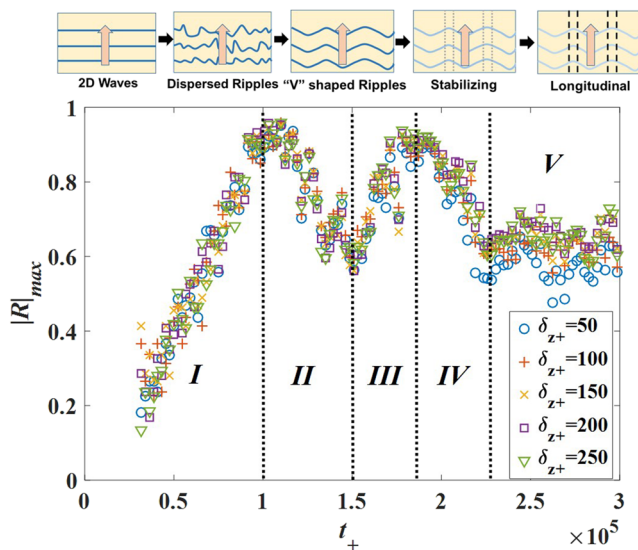
FIG. 20. Time-variation of $|R|_{max}$ at the different surface-normal distances during the dynamic sand wave/ripple formation process.

velocimetry (PTV/PIV) technique was also used to reveal the two-phase (i.e., air–sediment) flow fields during the dynamic sand wave/ripple formation process. The main findings derived in this study are as follows:

1. A complete description of the sand bedform evolution was achieved. The sand surface evolved from the initial random 3D sand wavelets to the 2D sand waves and further into the well-organized sequences of 3D chevron-shaped sand ripples that were separated by the longitudinal streaks.
2. The mechanisms of the sand bedform transition from 2D to 3D features were revealed. A discrepancy of the local sand wave propagation at different transverse locations was revealed based on the wavelet analysis of the sand bed height variations, which was suggested to contribute to the formation of the 3D chevron-shaped sand ripples. It was also found that while the sand bed morphology developed from the 2D sand waves to the 3D chevron-shaped sand ripples, the wavelength of the sand surface profiles would become longer, and the fluctuation amplitude would become smaller.
3. The interaction between the dynamically evolving sand surface profile and the near-bed air–sediment flow field was revealed in great details. It was found that the formation of the sand waves/ripples could dramatically affect the near-bed sand particle flow field, which is found to be in phase with the sand surface profiles. It was also found that both the gas-phase flow structures and the sand particle flow structures can be highly disturbed by the dynamically evolving sand waves/ripples. While the gas flow field is featured with more vortical structures and higher turbulence intensities, the sand particle flow field is highlighted by the alternating positive and negative velocity regions.
4. Five dominant phases were extracted and defined to describe a complete sand wave/ripple formation process. By calculating the cross-correlation between the sand bed surface pattern and the surface-normal sand velocity profiles at the different surface-normal distances, five development phases were defined during the sand wave/ripple formation process: (I) initial strengthening phase, (II) transition phase, (III) ripple-modulated re-strengthening phase, (IV) stabilizing phase, and (V) longitudinal phase.

2D-to-3D transition process of the sand surface morphology, the correlation between the sand surface profile and the sand flow field is significantly reduced due to the intense transverse shear flow over the sand bed. The dispersed 3D sand ripples are then merged into the larger chevron-shaped sand ripples as they propagated downstream, which is called the (III) ripple-modulated re-strengthening phase. During this process, the correlation between the sand surface profile and the sand flow field is found to be re-strengthened along with the development of the chevron-shaped sand ripple sequence. As the ripple-modulated sand surface morphology is fully developed, i.e., the (IV) stabilizing phase, the correlation between the sand surface profile and the sand flow field is found to be weakened gradually due to the decreasing amplitude of the sand ripples during the stabilization process. Along with the stabilization of the chevron-shaped sand ripple sequences, the longitudinal streaks are found to be formed [i.e., (V) longitudinal phase] due to the presence of counter-rotating quasi-streamwise vortices,[10] in which process the correlation between the sand surface profile and the sand flow velocity is almost not changed. Thus, a complete evolution process of the sand bed surface morphology as well as the near-bed flow field is well defined, which is of great importance to help understand the dynamic sand wave/ripple formation submerged in a turbulent boundary layer airflow.

VI. CONCLUSIONS

An experimental study was conducted to investigate the spatiotemporal evolution of the sand waves/ripples submerged in a turbulent boundary layer airflow. While a digital image projection (DIP) technique was applied to achieve temporally synchronized and spatially resolved measurements of the dynamically evolving sand surface morphology, a combined particle tracking/imaging

AUTHORS' CONTRIBUTIONS

Y.L. and X.J. contributed equally to this work.

ACKNOWLEDGMENTS

DATA AVAILABILITY

The data that support the findings of this study are available from the corresponding author upon reasonable request.

REFERENCES

[1] F. Charru, B. Andreotti, and P. Claudin, "Sand ripples and dunes," Annu. Rev. Fluid Mech. **45**, 469 (2013).

[2] B. Andreotti, P. Claudin, O. Devauchelle, O. Durán, and A. Fourrière, "Bedforms in a turbulent stream: Ripples, chevrons and antidunes," J. Fluid Mech. **690**, 94 (2012).

[3] G. H. Darwin, "I. On the formation of ripple-mark in sand," Proc. R. Soc. London **36**, 18 (1883).

[4] V. Cornish, "On the formation of sand-dunes," Geogr. J. **9**, 278 (1897).

[5] W. J. H. King, "The nature and formation of sand ripples and dunes," Geogr. J. **47**, 189 (1916).

[6] R. A. Bagnold, "The transport of sand by wind," Geogr. J. **89**, 409 (1937).

[7] R. P. Sharp, "Wind ripples," J. Geol. **71**, 617 (1963).

[8] P. K. Haff and B. T. Werner, "Computer simulation of the mechanical sorting of grains," Powder Technol. **48**, 239 (1986).

[9] B. T. Werner, "A steady-state model of wind-blown sand transport," J. Geol. **98**, 1 (1990).

[10] Y. Niño and M. H. Garcia, "Experiments on particle—Turbulence interactions in the near–wall region of an open channel flow: Implications for sediment transport," J. Fluid Mech. **326**, 285 (1996).

[11] R. A. Bagnold, *The Physics of Blown Sand and Desert Dunes* (Methuen, London, 1941).

[12] J. E. Ungar and P. K. Haff, "Steady state saltation in air," Sedimentology **34**, 289 (1987).

[13] R. A. Bagnold, "The flow of cohesionless grains in fluids," Philos. Trans. R. Soc., A **249**, 235 (1956).

[14] G. I. Wilson, "Aeolian bedforms—Their development and origins," Sedimentology **19**, 173 (2006).

[15] J. M. Ellwood, P. D. Evans, and I. G. Wilson, "Small scale aeolian bedforms," SEPM J. Sediment. Res. **45**, 554 (1975).

[16] R. S. Anderson, "Eolian ripples as examples of self-organization in geomorphological systems," Earth-Sci. Rev. **29**, 77 (1990).

[17] R. S. Anderson, "A theoretical model for aeolian impact ripples," Sedimentology **34**, 943 (1987).

[18] H.-K. Liu, "Mechanics of sediment-ripple formation," J. Hydraul. Div. **83**, 1 (1957).

[19] J. F. Kennedy, "The mechanics of dunes and antidunes in erodible-bed channels," J. Fluid Mech. **16**, 521 (1963).

[20] F. Engelund, "Instability of erodible beds," J. Fluid Mech. **42**, 225 (1970).

[21] K. J. Richards, "The formation of ripples and dunes on an erodible bed," J. Fluid Mech. **99**, 597 (1980).

[22] W. C. Kuru, D. T. Leighton, and M. J. McCready, "Formation of waves on a horizontal erodible bed of particles," Int. J. Multiphase Flow **21**, 1123 (1995).

[23] N. Zgheib and S. Balachandar, "Linear stability analysis of subaqueous bedforms using direct numerical simulations," Theor. Comput. Fluid Dyn. **33**, 161 (2019).

[24] H. T. Kim, S. J. Kline, and W. C. Reynolds, "The production of turbulence near a smooth wall in a turbulent boundary layer," J. Fluid Mech. **50**, 133 (1971).

[25] P. B. Williams and P. H. Kemp, "Initiation of ripples on flat sediment beds," J. Hydraul. Div. **97**, 502 (1971).

[26] R. G. Jackson, "Sedimentological and fluid-dynamic implications of the turbulent bursting phenomenon in geophysical flows," J. Fluid Mech. **77**, 531 (1976).

[27] J. Best, "On the entrainment of sediment and initiation of bed defects: Insights from recent developments within turbulent boundary layer research," Sedimentology **39**, 797 (1992).

[28] F. Sotiropoulos and A. Khosronejad, "Sand waves in environmental flows: Insights gained by coupling large-eddy simulation with morphodynamics," Phys. Fluids **28**, 021301 (2016).

[29] S. Dey, S. Sarkar, and L. Solari, "Near-bed turbulence characteristics at the entrainment threshold of sediment beds," J. Hydraul. Eng. **137**, 945 (2011).

[30] R. J. Hardy, J. L. Best, D. R. Parsons, and T. I. Marjoribanks, "On the evolution and form of coherent flow structures over a gravel bed: Insights from whole flow field visualization and measurement," J. Geophys. Res.: Earth Surf. **121**, 1472 (2016).

[31] W. Shih, P. Diplas, A. O. Celik, and C. Dancey, "Accounting for the role of turbulent flow on particle dislodgement via a coupled quadrant analysis of velocity and pressure sequences," Adv. Water Resour. **101**, 37 (2017).

[32] J. Groom and H. Friedrich, "Spatial structure of near-bed flow properties at the grain scale," Geomorphology **327**, 14 (2019).

[33] S. Dey, P. Paul, H. Fang, and E. Padhi, "Hydrodynamics of flow over two-dimensional dunes," Phys. Fluids **32**, 025106 (2020).

[34] V. I. Nikora and D. G. Goring, "Sand waves in unidirectional flows: Scaling and intermittency," Phys. Fluids **12**, 703 (2000).

[35] T. Pähtz, O. Durán, T.-D. Ho, A. Valance, and J. F. Kok, "The fluctuation energy balance in non-suspended fluid-mediated particle transport," Phys. Fluids **27**, 013303 (2015).

[36] Y. Liu, H. Fang, L. Huang, and G. He, "Numerical simulation of the production of three-dimensional sediment dunes," Phys. Fluids **31**, 096603 (2019).

[37] D. Berzi and L. Fraccarollo, "Intense sediment transport: Collisional to turbulent suspension," Phys. Fluids **28**, 023302 (2016).

[38] X. J. Zheng, T. L. Bo, and L. Xie, "DPTM simulation of aeolian sand ripple," Sci. China, Ser. G: Phys., Mech. Astron. **51**, 328 (2008).

[39] O. Durán, P. Claudin, and B. Andreotti, "Direct numerical simulations of aeolian sand ripples," Proc. Natl. Acad. Sci. U. S. A. **111**, 15665 (2014).

[40] Y. Liu, W.-L. Chen, L. J. Bond, and H. Hu, "An experimental study on the characteristics of wind-driven surface water film flows by using a multi-transducer ultrasonic pulse-echo technique," Phys. Fluids **29**, 012102 (2017).

[41] Y. Liu, L. J. Bond, and H. Hu, "Reconstruction of wave features in wind-driven water film flow using ultrasonic pulse-echo technique," AIP Conf. Proc. **1706**, 020015 (2016).

[42] A. Benetazzo, "Measurements of short water waves using stereo matched image sequences," Coast. Eng. **53**, 1013 (2006).

[43] J. Salvi, S. Fernandez, T. Pribanic, and X. Llado, "A state of the art in structured light patterns for surface profilometry," Pattern Recognit. **43**, 2666 (2010).

[44] H. Hu, B. Wang, K. Zhang, W. Lohry, and S. Zhang, "Quantification of transient behavior of wind-driven surface droplet/rivulet flows using a digital fringe projection technique," J. Visualization **18**, 705 (2014).

[45] K. Zhang, T. Wei, and H. Hu, "An experimental investigation on the surface water transport process over an airfoil by using a digital image projection technique," Exp. Fluids **56**, 173 (2015).

[46] Y. Liu, K. Zhang, W. Tian, and H. Hu, "An experimental study to characterize the effects of initial ice roughness on the wind-driven water runback over an airfoil surface," Int. J. Multiphase Flow **126**, 103254 (2020).

[47] J. H. M. Fransson, "Leading edge design process using a commercial flow solver," Exp. Fluids **37**, 929 (2004).

[48] F. Scarano and M. L. Riethmuller, "Advances in iterative multigrid PIV image processing," Exp. Fluids **29**, S051–S060 (2000).

[49] R. Theunissen, A. Stitou, and M. L. Riethmuller, "A novel approach to improve the accuracy of PTV methods," in *12th International Symposium on Applications of Laser Techniques to Fluid Mechanics, Lisbon, Portugal* (Springer-Verlag, 2004), pp. 12–15.

[50] Y. Wu, "A study of energetic large-scale structures in turbulent boundary layer," Phys. Fluids **26**, 045113 (2014).

[51] R. D. Moser and P. Moin, "Characteristic-eddy decomposition of turbulence in a channel," J. Fluid Mech. **200**, 471 (1989).

[52] L. H. O. Hellström and A. J. Smits, "Structure identification in pipe flow using proper orthogonal decomposition," Philos. Trans. R. Soc., A **375**, 20160086 (2017).

[53] J. D. Kulick, J. R. Fessler, and J. K. Eaton, "Particle response and turbulence modification in fully developed channel flow," J. Fluid Mech. **277**, 109 (1994).

[54] A. Aliseda, A. Cartellier, F. Hainaux, and J. C. Lasheras, "Effect of preferential concentration on the settling velocity of heavy particles in homogeneous isotropic turbulence," J. Fluid Mech. **468**, 77 (2002).

[55] H.-Y. Zhu, C. Pan, J.-J. Wang, Y.-R. Liang, and X.-C. Ji, "Sand-turbulence interaction in a high-Reynolds-number turbulent boundary layer under net sedimentation conditions," Int. J. Multiphase Flow **119**, 56 (2019).

[56] A. Poortinga, J. van Minnen, J. Keijsers, M. Riksen, D. Goossens, and M. Seeger, "Measuring fast-temporal sediment fluxes with an analogue acoustic sensor: A wind tunnel study," PLoS One **8**, e74007 (2013).

[57] H. Tsoar, "Bagnold, R.A. 1941: The physics of blown sand and desert dunes. London: Methuen," Prog. Phys. Geogr.: Earth Environ. **18**, 91 (1994).

[58] Y. Shao and H. Lu, "A simple expression for wind erosion threshold friction velocity," J. Geophys. Res.: Atmos. **105**, 22437, https://doi.org/10.1029/2000jd900304 (2000).

[59] R. Greeley and J. D. Iversen, *Wind as a Geological Process* (Cambridge University Press, Cambridge, 1985).

[60] J. F. Kok and N. O. Renno, "A comprehensive numerical model of steady state saltation (COMSALT)," J. Geophys. Res.: Atoms. **114**, D17204 (2009).

[61] D. J. Tritton, *Physical Fluid Dynamics* (Springer Science & Business Media, 2012).

[62] A. G. Kidanemariam and M. Uhlmann, "Formation of sediment patterns in channel flow: Minimal unstable systems and their temporal evolution," J. Fluid Mech. **818**, 716 (2017).

[63] S. Shahinfar and J. H. M. Fransson, "Effect of free-stream turbulence characteristics on boundary layer transition," J. Phys.: Conf. Ser. **318**, 032019 (2011).

[64] A. J. Musker, "Explicit expression for the smooth wall velocity distribution in a turbulent boundary layer," AIAA J. **17**, 655 (1979).

[65] D. B. Spalding, "A single formula for the "law of the wall"," J. Appl. Mech. Trans. **28**, 455 (1961).

[66] T. B. Nickels, "Inner scaling for wall-bounded flows subject to large pressure gradients," J. Fluid Mech. **521**, 217 (2004).

[67] J. F. Kok, E. J. R. Parteli, T. I. Michaels, and D. B. Karam, "The physics of wind-blown sand and dust," Rep. Prog. Phys. **75**, 106901 (2012).

[68] S. E. Coleman and B. W. Melville, "Initiation of bed forms on a flat sand bed," J. Hydraul. Eng. **122**, 301 (1996).

[69] C. Lee and R. Li, "Dominant structure for turbulent production in a transitional boundary layer," J. Turbul. **8**, N55 (2007).

[70] S. E. Coleman and V. I. Nikora, "Bed and flow dynamics leading to sediment-wave initiation," Water Resour. Res. **45**, W04402, https://doi.org/10.1029/2007wr006741 (2009).

[71] D. Yang and L. Shen, "Characteristics of coherent vortical structures in turbulent flows over progressive surface waves," Phys. Fluids **21**, 125106 (2009).

[72] J. M. Lilly and S. C. Olhede, "Generalized morse wavelets as a superfamily of analytic wavelets," IEEE Trans. Signal Process. **60**, 6036 (2012).

[73] H. Tennekes and J. L. Lumley, *A First Course in Turbulence* (MIT Press, 1972).